MNRAS 000, 1–20 (2019) Preprint 27 November 2019 Compiled using MNRAS LATEX style file v3.0

# ALMA and ROSINA detections of phosphorus-bearing molecules: the interstellar thread between star-forming regions and comets

V. M. Rivilla[1]⋆, M. N. Drozdovskaya[2], K. Altwegg[3], P. Caselli[4], M. T. Beltrán[1], F. Fontani[1], F.F.S. van der Tak[5,6], R. Cesaroni[1], A. Vasyunin[7,8], M. Rubin[2], F. Lique[9], S. Marinakis[10,11], L. Testi[1,12,13], and the ROSINA team[14]
*The full list of affiliations appears at the end of the paper in Appendix A.*





Accepted 2019 November 21. Received 2019 October 29; in original form 2019 August 8.

## ABSTRACT

To understand how Phosphorus-bearing molecules are formed in star-forming regions, we have analysed ALMA observations of PN and PO towards the massive star-forming region AFGL 5142, combined with a new analysis of the data of the comet 67P/Churyumov-Gerasimenko taken with the ROSINA instrument onboard *Rosetta*. The ALMA maps show that the emission of PN and PO arises from several spots associated with low-velocity gas with narrow linewidths in the cavity walls of a bipolar outflow. PO is more abundant than PN in most of the spots, with the PO/PN ratio increasing as a function of the distance to the protostar. Our data favor a formation scenario in which shocks sputter phosphorus from the surface of dust grains, and gas-phase photochemistry induced by UV photons from the protostar allows efficient formation of the two species in the cavity walls. Our analysis of the ROSINA data has revealed that PO is the main carrier of P in the comet, with PO/PN>10. Since comets may have delivered a significant amount of prebiotic material to the early Earth, this finding suggests that PO could contribute significantly to the phosphorus reservoir during the dawn of our planet. There is evidence that PO was already in the cometary ices prior to the birth of the Sun, so the chemical budget of the comet might be inherited from the natal environment of the Solar System, which is thought to be a stellar cluster including also massive stars.

**Key words:** astrochemistry – ISM:molecules – molecular data – comets:general – stars:formation

## 1 INTRODUCTION

Phosphorus (P) is a key chemical biogenic element for the development of life (Gulick 1955, Maciá et al. 1997, Schwartz 2006, Gamoke et al. 2009, Fernández-García et al. 2017). While the cosmic abundance of P in the Universe is low relative to hydrogen, P/H $\sim 3\times10^{-7}$ (Grevesse & Sauval 1998, Asplund et al. 2009), its abundance in living organisms is several orders of magnitude higher, e.g., P/H $\sim 10^{-3}$ in bacteria (e.g., Fagerbakke et al. 1996). P-compounds are unique in forming large biomolecules, thanks to their extreme structural stability and functional reactivity. Phosphorus is one of the crucial components of deoxyribonucleic acid (DNA) and ribonucleic acid (RNA), phospholipids (the structural components of cellular membranes) and the adenosine triphosphate (ATP) molecule, which stores and transports chemical energy within cells (see, e.g., Pasek & Lauretta 2005). Moreover, P-compounds have been proposed as key catalysts and chemical buffers for the formation of nucleotides (Powder et al. 2009). All of this makes P one of the major limiting nutrient for the development of life (Redfield 1958), and may make P-bearing molecules important biomarkers in exoplanets (Sousa-Silva et al. 2019). A fundamental question is how the reservoir of P became biologically available on planets, and in particular on the early Earth. In this regard, two research directions can be pursued from the astrophysical/astrochemical point of view. On the one hand, one can study the chemical composition of the interstellar medium (ISM) of the parental molecular clouds that form new stars and planets. On the other hand, one can investigate the chemical compounds of objects found in our Solar System, such as meteorites and comets, which may have delivered prebiotic chemicals to our early Earth.

The chemistry of P in the ISM is poorly understood. P is a relatively heavy element (atomic mass of 31 Da), and is thought to be synthesized in massive stars and injected into the ISM through supernova explosions (Koo et al. 2013). As pointed out by Maciá et al. (1997), the low number of these massive stars may explain the rel-

⋆ E-mail: rivilla@arcetri.astro.it

atively low cosmic abundance of P relative to hydrogen. Moreover, until very recently, it was thought that P is heavily depleted on the surfaces of insterstellar dust grains in the dense and cold interstellar medium by factors of $600-10^4$ (e.g., Turner et al. 1990, Wakelam & Herbst 2008). This would make the detection of P-bearing molecules in the gas phase through the conventional rotational spectroscopy difficult. Indeed, unlike other biogenic elements (C, N, O, S), P is barely detected in the ISM. The ion $P^+$ was detected in several diffuse clouds (Jura & York 1978), and only a few simple P-bearing species (PN, PO, CP, HCP, $C_2P$, $PH_3$) have been identified towards the circumstellar envelopes of evolved stars (Guelin et al. 1990; Agúndez et al. 2007; Tenenbaum et al. 2007, Milam et al. 2008, Halfen et al. 2008, De Beck et al. 2013, Agúndez et al. 2014, Ziurys et al. 2018). In star-forming regions, only PN was detected before 2016 towards a handful of sources (Turner & Bally 1987; Ziurys 1987; Turner et al. 1990; Caux et al. 2011; Yamaguchi et al. 2011). In the last years, a considerable step forward has been made. Since there is growing evidence that out Solar System was born in a warm and massive dense core with high-mass stars (Adams 2010, Pfalzner et al. 2015, Taquet et al. 2016, Drozdovskaya et al. 2018, Lichtenberg et al. 2019), several works have been devoted to studying P-bearing molecules in massive cores, whose chemistry may be inherited by future Solar-like systems. The molecule PN has been detected in other massive star-forming regions (Fontani et al. 2016; Mininni et al. 2018; Fontani et al. 2019), and PO has been detected for the first time in two massive star-forming regions, with an abundance ratio of PO/PN in the range of 1.8−3 (Rivilla et al. 2016). Afterwards, new detections of PO in shocked material (Lefloch et al. 2016; Rivilla et al. 2018; Bergner et al. 2019) have confirmed that PO seems to be more abundant than PN in the ISM.

The relatively low number of detections of PN and PO have prevented so far a good understanding of its formation. Three main mechanisms have been proposed: (i) shock-induced formation (Yamaguchi et al. 2011; Aota & Aikawa 2012; Lefloch et al. 2016; Rivilla et al. 2018; Mininni et al. 2018); (ii) high-temperature gas-phase chemistry (Charnley & Millar 1994); and (iii) gas-phase formation during the cold collapse phase of the parental core (Rivilla et al. 2016). To date, this debate has been strongly limited due to the lack of information about the spatial distribution of the emission of P-bearing molecules in star-forming regions. Therefore, interferometric maps of P-bearing molecules are needed to discriminate among the different proposed mechanisms.

The knowledge about P in our Solar System is also limited due to the low number of detections. Phosphine, $PH_3$, has been observed in the atmospheres of Jupiter and Saturn (Bregman et al. 1975, Ridgway et al. 1976, Larson et al. 1977, Weisstein & Serabyn 1994, Irwin et al. 2004, Fletcher et al. 2009); and P has been identified in meteorites in the form of the mineral schreibersite (Pasek & Lauretta 2005) and phosphoric acids (Schwartz 2006). Traces of P may have been present in the dust of comet Halley, but it was not identified in Stardust grains of comet Wild 2 (Macia 2005). More recently, the in-situ measurements of the *Rosetta* mission claimed the presence of P in the comet 67P/Churyumov-Gerasimenko (67P/C-G, hereafter; Altwegg et al. 2016), although the parent molecule(s) could not be determined.

In this work, we combine the search for P-bearing molecules in the star-forming region AFGL 5142 using the Atacama Large Millimeter/Submillimeter Array (ALMA) with new analysis of the data of the coma of the comet 67P/C-G taken with the *Rosetta* Orbiter Spectrometer for Ion and Neutral Analysis (ROSINA) instrument. This comparison will allow us to establish if the pristine chemical composition of the comet, in particular the P-bearing reservoir, may have been inherited from a parental molecular core similar to the one that formed our Sun.

AFGL 5142 is a star-forming region in the Perseus arm, where low-mass and high-mass star formation is ongoing simultaneously (Hunter et al. 1999). It is located at a relatively close distance, 2.14 kpc (Burns et al. 2017), which allows us to study the molecular emission at high spatial resolution. Several $H_2O$ and $CH_3OH$ masers have been identified in the region (Hunter et al. 1995; Goddi & Moscadelli 2006; Goddi et al. 2007). The center of the region harbors a dust millimeter core (MM position, hereafter, see Fig. 1) detected by Hunter et al. (1999), which actually consists of five millimeter sources, some of them associated with hot cores with high temperatures in the range of 90−250 K (Zhang et al. 2007). Hunter et al. (1999) detected a SiO outflow in the northeast-southwest direction powered by this central protocluster. Observations of other molecular species such as CO, HCN, $HCO^+$ (Zhang et al. 2007; Liu et al. 2016) confirmed the presence of abundant shocked material. Busquet et al. (2011) revealed, based on observations of $N_2H^+$, the presence of a cold starless core located ∼12″ to the west (see Fig. 1). Several PN transitions have been detected with single-dish observations (Fontani et al. 2016; Mininni et al. 2018). The presence of varied physical conditions in a single region makes AGFL 5142 a well suitable laboratory to test the different mechanisms proposed for the formation of P-bearing species. It harbours three different environments where each mechanism could be dominant: i) a system of low- and high-mass protostars whose heating produces a chemically-rich molecular hot core (gas-phase chemistry scenario); ii) abundant shocked material produced by outflowing material (Zhang et al. 2002; Liu et al. 2016; shock scenario); and iii) a starless cold core (Busquet et al. 2011; cold collapse scenario).

67P/C-G is a Jupiter-family comet with a period of ∼6.5 years. Several studies suggested that it experienced a close encounter with Jupiter in February 1959, which reduced its perihelion distance from 2.7 to the current 1.2 au (Lamy et al. 2007). Its nucleus has a bilobate shape and is approximately 4.3×2.6×2.1 km in size (Jorda et al. 2016). The *Rosetta* mission escorted the comet pre- and post-its August 2015 perihelion passage, revealing that the dusty surface covers an icy interior (Fornasier et al. 2016). The most recent analysis of mission data suggest that 67P/C-G is indeed a primordial rubble pile containing non-thermally processed materials that were once part of the protoplanetary disk that evolved into our modern-day Solar System (e.g., Altwegg et al. 2015; Davidsson et al. 2016; Alexander et al. 2018).

This work is organised as follows. In Section 2 we present the ALMA and ROSINA data. We present our results in Section 3 and discuss their implications for the formation of P-bearing molecules in star- and planet-forming regions in Section 4. Finally, we summarize our main findings in Section 5.

## 2 OBSERVATIONS

### 2.1 ALMA observations

We carried out interferometric observations using 40 antennas of the Atacama Large Millimeter/Submillimeter Array (ALMA) in Cycle 4 between January and April of 2017 as part of the project 2016.1.01071.S (PI: Rivilla). The phase center was RA= 5h 30m 48.0s, DEC=33° 47′ 54.0″. The observations were performed in Band 3 with the array in the C40−3 configuration with baselines ranging from 15 to 460 m. The digital correlator was configured in 12 different spectral windows (spw's) with channel widths of

**Table 1.** Molecular transitions studied in this ALMA dataset, from the CDMS molecular database.

| Molecule | Transition | Frequency (GHz) | log$A_{ij}$ ($s^{-1}$) | $E_{up}$ (K) |
|---|---|---|---|---|
| PN | N=2−1, J=2−2 | 93.9782 | -5.13724 | 6.8 |
| PN | N=2−1, J=1−0 | 93.9785 | -4.79039 | 6.8 |
| PN | N=2−1, J=2−1 | 93.9798 | -4.66014 | 6.8 |
| PN | N=2−1, J=3−2 | 93.9799 | -4.53516 | 6.8 |
| PN | N=2−1, J=1−2 | 93.9808 | -6.09138 | 6.8 |
| PN | N=2−1, J=1−1 | 93.9823 | -4.91538 | 6.8 |
| PO | J=5/2−3/2, Ω=1/2, F=3−2, l=e | 108.9984 | -4.67162 | 8.4 |
| PO | J=5/2−3/2, Ω=1/2, F=2−1, l=e | 109.0454 | -4.71670 | 8.4 |
| PO | J=5/2−3/2, Ω=1/2, F=3−2, l=f | 109.2062 | -4.69959 | 8.4 |
| PO | J=5/2−3/2, Ω=1/2, F=2−1, l=f | 109.2812 | -4.71444 | 8.4 |
| SO | N=2−1, J=3−2 | 109.2522 | -4.95802 | 21.1 |

**Table 2.** Coordinates of the positions in the AFGL 5142 region studied in this work.

| Position Position | RA (J2000) h : m : s | DEC (J2000) ° : ′ : ″ |
|---|---|---|
| P1 | 05:30:48.38 | 33:48:14.5 |
| P2 | 05:30:48.18 | 33:47:45.1 |
| P3 | 05:30:47.45 | 33:47:43.1 |
| P4 | 05:30:47.09 | 33:47:36.3 |
| P5 | 05:30:49.54 | 33:47:35.7 |
| P6 | 05:30:49.78 | 33:47:33.3 |
| P7 | 05:30:49.86 | 33:47:30.3 |
| MM | 05:30:48.02 | 33:47:54.2 |
| SC | 05:30:48.95 | 33:47:52.9 |
| HV-b | 05:30:47.83 | 33:47:47.3 |
| HV-r | 05:30:48.12 | 33:48:00.2 |

122 kHz (∼0.35 km $s^{-1}$), which cover the PN(2−1) transition, the J=5/2−3/2, Ω=1/2 quadruplet of PO, and the SO $2_3-1_2$ transition (see Table 1). The precipitable water vapor (pwv) during the observations was in the range of 1.5−5.6 mm. Flux and bandpass calibration were obtained through observations of J0510+1800. The phase was calibrated by observing J0547+2721 and J0552+3754. The on-source observing time was about 2.5 hr. The synthesized beams are 2.5″×1.8″ for the PN map, and 2.1″×1.6″ for the PO and SO maps. The root mean square (*rms*) of the noise of the maps is ∼2 mJy $beam^{-1}$ per channel. The data were calibrated and imaged using standard ALMA calibration scripts of the Common Astronomy Software Applications package (CASA)[1]. Further analysis was done with MADCUBA[2] software package (Martín et al. 2019).

### 2.2 ROSINA measurements

The *Rosetta* spacecraft of the European Space Agency (Glassmeier et al. 2007) accompanied the comet 67P/C-G during two years from August 2014 through September 2016. On-board *Rosetta* was the instrument suite *Rosetta* Orbiter Sensor for Ion and Neutral Analysis (ROSINA) with two mass spectrometers and a pressure sensor (Balsiger et al. 2007). During the two weeks on October 2014, at a distance of 3 au from the Sun, but only 10 km from the nucleus, the densities measured in the coma by ROSINA DFMS (Double Focusing Mass Spectrometer) were relatively high allowing the detection of low-abundance species. DFMS measures one integer mass with a resolution of ∼9000 at full width half maximum (FWHM) at mass 28 Da at a time. The integration time is 20 s. The detector has a one-dimensional array of 512 pixels. A peak can be well approximated by a double Gaussian, whereby the second Gaussian has a ∼3 times larger width and a 10 times lower height. For small peaks, one Gaussian is precise enough for most purposes. All peaks on one integer mass have the same widths for the two Gaussians. Details on the data analysis can be found in Le Roy et al. (2015) and Calmonte et al. (2016).

## 3 ANALYSIS AND RESULTS

### 3.1 ALMA maps of the AFGL5142 star-forming region

#### *3.1.1 Spatial distribution and kinematics of SO: a bipolar outflow cavity*

With the aim of interpreting in the following section the maps of PN and PO, we first discuss here the spatial distribution and kinematics of the $2_3-1_2$ transition of SO. Our maps exhibit SO emission from velocities of −12 km $s^{-1}$ to +6 km $s^{-1}$ (the systemic velocity of the central core is −2.85 km $s^{-1}$). We show in Fig. 1 the maps of SO: panel *a* includes all velocities, while panel *b* includes only the highest velocities with respect the systemic velocity. The SO emission peaks towards the MM position, but also traces extended structures distributed across the field of view. Since SO is considered a good tracer of shocked material (e.g., Martin-Pintado et al. 1992; Pineau des Forets et al. 1993; Chernin et al. 1994; Bachiller & Pérez Gutiérrez 1997; Podio et al. 2015), we interpret the SO emission in terms of shocked (or post-shocked, see below) material produced by an outflow driven by a central protostar.

Zhang et al. (2007) and Liu et al. (2016) interpreted previous observations of CO, HCN and $HCO^+$ as a system of up to three different outflows arising from the central protostar(s). Although this hypothesis is plausible, we propose that the SO emission is tracing the cavities of a single wide-angle bipolar outflow (see overplotted dashed lines in Fig. 1). The redshifted and blueshifted high velocity SO emission (Fig. 1b) traces very well the launching point of the molecular outflow, coinciding with the central protostar, and the northeast-southwest direction of the bipolar outflow in the plane of the sky (see zoom-in view in the central inset of Fig. 1b). This direction of the bipolar outflow is also in good agreement with the elongated morphology of the Spitzer-IRAC2[3] emission at 4.5 $\mu$m (inset in Fig. 1b), which is a good tracer of shocked $H_2$ emission in protostellar outflows (e.g., Smith & Rosen 2005; Qiu et al. 2008), and with the SiO bipolar outflow detected by Hunter et al. (1999). The interaction of the lobes of the outflow with the surrounding gas might be responsible for the gas heating observed by Zhang et al. (2002, 2007) using several inversion transitions of $NH_3$ (see Fig. 1c; Zhang, priv. comm.). The detected hot spots towards the northeast and south/southwest are in good agreement with the direction of

[1] https://casa.nrao.edu

[2] Madrid Data Cube Analysis on ImageJ is a software developed in the Center of Astrobiology (Madrid, INTA-CSIC) to visualize and analyze astronomical single spectra and datacubes. MADCUBA is available at http://cab.inta-csic.es/madcuba/Portada.html

[3] Spitzer-IRAC2 image obtained from the NASA/IPAC Infrered Science Archive: https://irsa.ipac.caltech.edu/Missions/spitzer.html

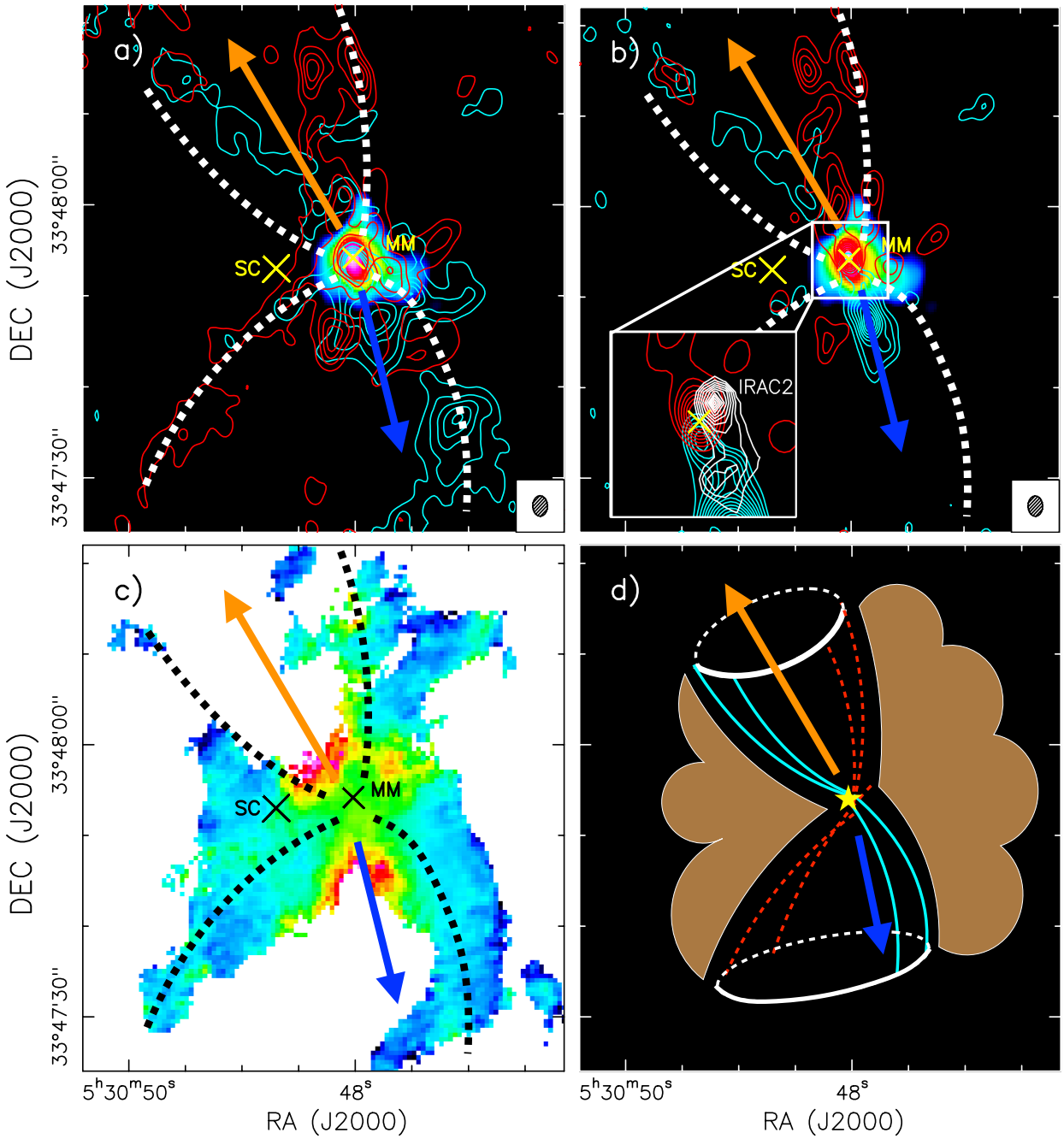


**Figure 1.** a) ALMA maps of the SO($2_3-1_2$) transition. We show two different velocity ranges: [-12,-4] km s$^{-1}$ (light blue contours) and [-3.5, 6] km s$^{-1}$ (red contours). The contour levels start at 40/50 mJy km s$^{-1}$ beam$^{-1}$ and increase in steps of 75/100 mJy km s$^{-1}$ beam$^{-1}$ for the blushifted/redshifted emission. The continuum map is shown in color scale, starting from blue (~2 mJy beam$^{-1}$) to magenta (30 mJy beam$^{-1}$). The beam of the continuum map (2.27″×1.65″) is indicated in the lower right corner. The cavity of the bipolar outflow is indicated with dashed white curves, and the direction of the redshifted/blushifted lobes of the bipolar outflow are indicated with orange/blue arrows, respectively. The positions of the MM core and the starless core (SC) are indicated with yellow crosses. b) Same as in panel a), but showing only the high velocity gas: [0.5,6] km s$^{-1}$ (red) and [-12,-7.5] km s$^{-1}$ (light blue). The contour levels start at 20/50 mJy km s$^{-1}$ beam$^{-1}$ and increase in steps of 25/50 mJy km s$^{-1}$ beam$^{-1}$ for the blushifted/redshifted emission. The inset in the lower left shows a zoom-in of the inner region. In the inset, the contour levels start at 30/100 mJy km s$^{-1}$ beam$^{-1}$ and increase in steps of 10/50 mJy km s$^{-1}$ beam$^{-1}$ for the blushifted/redshifted emission. The emission at 4.5 $\mu$m from Spitzer−IRAC2 is overplotted in white contours. c) Ratio between the emission of $NH_3$ (J,K) = (3,3) to (J,K) = (1,1), adapted from Zhang et al. (2002) (see this work for futher details). The color scale is a proxy of the gas temperature: red is hotter and dark blue is cooler. The gas is heated at the base of the two molecular outflow cavities. d) Schematic picture of the region. The bipolar outflow is close to the plane of the sky, and it is excavating two cavities in the natal molecular core.

**Table 3.** Results of the LTE analysis of the PN, PO and SO transitions detected towards the different AFGL 5142 positions studied in this work. Some of the positions exhibit several velocity components (different rows in this table).

| Region | PN | | | | PO | | | | SO | | | |
|---|---|---|---|---|---|---|---|---|---|---|---|---|
| | $N$ ($\times10^{12}$ cm$^{-2}$) | $v_{\rm LSR}$ (km s$^{-1}$) | $\Delta v$ (km s$^{-1}$) | $\tau^{(a)}$ | $N$ ($\times10^{12}$ cm$^{-2}$) | $v_{\rm LSR}$ (km s$^{-1}$) | $\Delta v$ (km s$^{-1}$) | $\tau^{(a)}$ | $N$ ($\times10^{14}$ cm$^{-2}$) | $v_{\rm LSR}$ (km s$^{-1}$) | $\Delta v$ (km s$^{-1}$) | $\tau^{(a)}$ |
| P1 | 1.8±0.2 | -0.8±0.2 | 2.6±0.3 | 0.047±0.006 | < 2.0 | -0.8 | 2.6 | - | 3.8±0.2 | -1.53±0.04 | 3.8±0.2 | 0.048±0.001 |
| | < 0.3 | 2.1 | 7.1 | - | < 3.3 | 2.1 | 7.1 | - | 1.84±0.08 | 2.1±0.2 | 7.1±0.4 | 0.012±0.001 |
| P2 | 3.1±0.2 | -2.1±0.2 | 5.0±0.4 | 0.041±0.004 | 1.7±0.6 | -2.1 | 5.0 | 0.002±0.001 | 5.25±0.06 | -2.1±0.1 | 5.8±0.1 | 0.043±0.001 |
| | < 0.4 | -1.97 | 2.0 | - | < 0.1 | -1.97 | 2.0 | - | 1.78±0.05 | -1.97±0.03 | 2.05±0.07 | 0.042±0.001 |
| | < 0.2 | -3.76 | 1.0 | - | < 0.1 | -3.76 | 1.0 | - | 0.68±0.03 | -3.76±0.03 | 1.05±0.06 | 0.031±0.002 |
| | < 0.2 | -6.2 | 1.7 | - | < 0.1 | -6.2 | 1.7 | - | 0.40±0.02 | -6.2±0.05 | 1.7±0.1 | 0.011±0.001 |
| P3 | 2.3±0.2 | -3.47±0.04 | 1.69±0.09 | 0.092±0.006 | 3.1±0.3 | -3.04±0.06 | 1.4±0.2 | 0.012±0.002 | 3.5±0.2 | -3.21±0.04 | 1.69±0.09 | 0.099±0.007 |
| P4 | 5.5±0.2 | -5.14±0.03 | 1.50±0.05 | 0.24±0.01 | 8.8±0.6 | -4.68±0.04 | 1.2±0.1 | 0.040±0.006 | 5.8±0.2 | -4.66±0.03 | 1.29±0.06 | 0.22±0.02 |
| P5 | 2.4±0.2 | -3.49±0.04 | 1.16±0.09 | 0.14±0.02 | 6.2±0.8 | -3.25±0.05 | 1.1±0.2 | 0.031±0.006 | 1.71±0.09 | -3.12±0.03 | 0.92±0.06 | 0.088±0.007 |
| P6 | 2.2±0.2 | -3.26±0.05 | 1.3±0.2 | 0.12±0.02 | 4.8±0.8 | -2.77±0.06 | 0.9±0.2 | 0.031±0.006 | 1.6±0.2 | -2.81±0.04 | 1.0±0.1 | 0.08±0.01 |
| P7 | 1.3±0.3 | -3.3±0.2 | 1.7±0.3 | 0.11±0.03 | < 1.2 | - | - | - | 1.10±0.06 | -3.03±0.03 | 0.94±0.07 | 0.055±0.004 |
| MM | 0.8±0.1 | -3.9±0.3 | 3.9±0.7 | 0.031±0.007 | < 0.6 | -3.9 | 3.9 | - | 28.0±0.6 | -2.85±0.05 | 4.7±0.1 | 0.278±0.009 |
| HV-b | < 0.18 | -4.1 | 2.1 | - | < 0.4 | -4.1 | 2.1 | - | 1.92±0.08 | -4.07±0.05 | 2.1±0.1 | 0.044±0.003 |
| | < 0.35 | -7.9 | 6.1 | - | < 0.6 | -7.9 | 6.1 | - | 4.62±0.08 | -7.95±0.05 | 6.1±0.2 | 0.035±0.001 |
| HV-r | < 0.16 | -3.96 | 4.85 | - | < 0.5 | -3.96 | 4.85 | - | 3.21±0.05 | -3.96±0.04 | 4.85±0.09 | 0.031±0.001 |
| | < 0.28 | -4.22 | 6.2 | - | < 0.3 | -4.22 | 6.2 | - | 2.78±0.07 | 4.22±0.07 | 6.2±0.2 | 0.021±0.001 |
| | < 0.32 | -0.21 | 1.5 | - | < 0.6 | -0.21 | 1.5 | - | 0.32±0.04 | 0.21±0.05 | 1.5±0.2 | 0.010±0.002 |

$^{(a)}$ Opacity of the hyperfine transition with highest $\tau$.

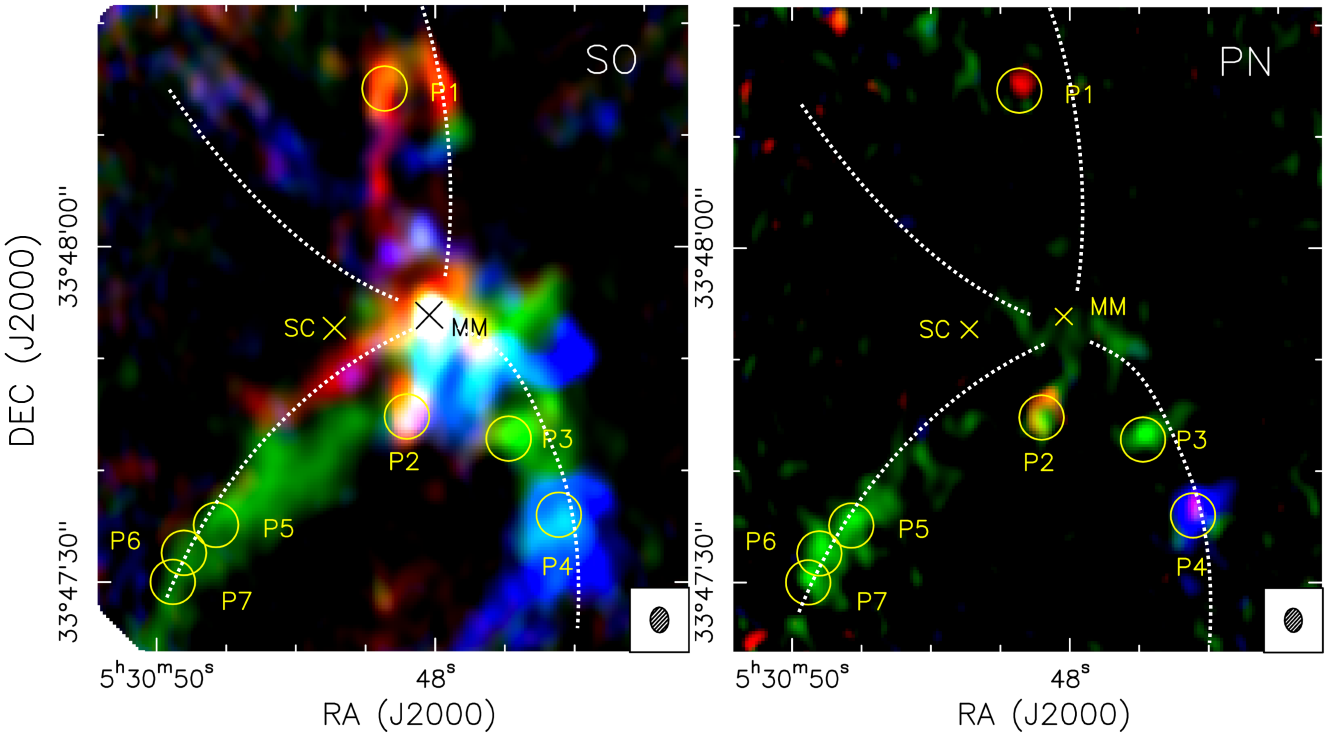


**Figure 2.** ALMA integrated maps of SO($2_3-1_2$) (left) and PN(2−1) (right) in three velocity ranges [-6.5,-4.5] km s$^{-1}$ (blue); [-4.5,-2.0] km s$^{-1}$ (green); [-2.0, 0] km s$^{-1}$ (red). The cavity of the bipolar outflow is indicated with dashed white curves. The positions of the starless core (SC) and the MM core are indicated with yellow (or black) crosses. The different P-spots (P1−P7) are identified with yellow circles. The beams of the observations are indicated in the lower right corner of each panel.

**Table 4.** Molecular abundance ratios at the AFGL 5142 positions and in the comet 67P/C-G. Different rows in a single position correspond to the different velocity components shown in Table 3.

| | PO/PN | SO/PN | SO/PO |
|---|---|---|---|
| AFGL 5142 positions | | | |
| P1 | < 1.1 | 207±9 | >195 |
| | - | > 650 | >57 |
| P2 | 0.6±0.2 | 170±11 | 309±107 |
| | - | > 470 | >1573 |
| | - | > 340 | >1202 |
| | - | > 200 | >707 |
| P3 | 1.4±0.3 | 151±14 | 112±17 |
| P4 | 1.6±0.2 | 107±7 | 66±7 |
| P5 | 2.6±0.6 | 72±9 | 27±5 |
| P6 | 2.2±0.6 | 70±12 | 33±10 |
| P7 | < 0.9 | 84±18 | >90 |
| MM | < 0.8 | 3370±580 | >4498 |
| HV-b | - | > 1057 | >522 |
| | - | 1303 | > 778 |
| HV-r | - | > 2042 | >630 |
| | - | > 979 | >983 |
| | - | > 101 | >57 |
| comet 67P/Churyumov-Gerasimenko | | | |
| | >10 | >60 | ~6 |

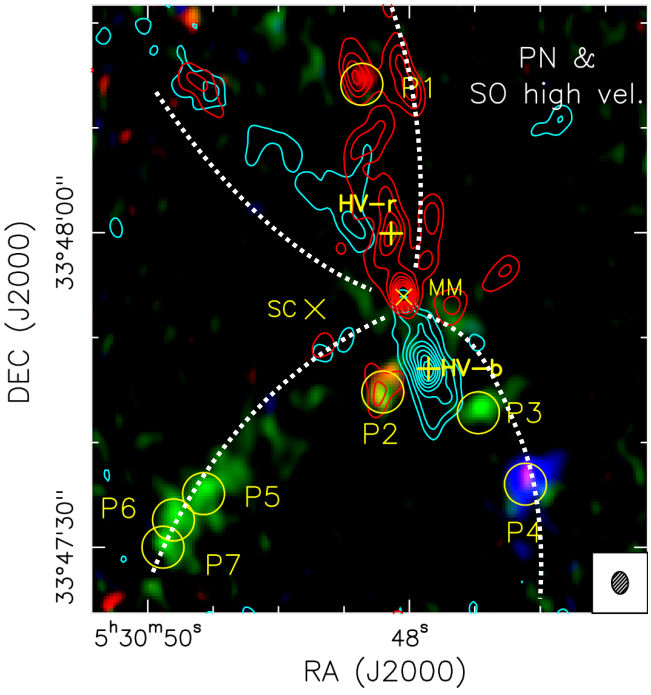


**Figure 3.** ALMA integrated PN(2−1) emission map (in colours) as shown in the right panel of Fig. 2, with the high velocity SO emission (in contours) shown in Fig. 1b overplotted. The positions of the starless core (SC) and the MM core are indicated with yellow crosses. The different P-spots (P1−P7) are identified with yellow circles. The positions of the high-velocity spots HV-r and HV-b are indicated with yellow plus signs. The cavity of the bipolar outflow is indicated with dashed white curves.

the bipolar outflow. This suggests that the mechanical energy of the outflow has opened two cavities in the parental core. SO and $NH_3$ mainly trace the interface of these cavities with the local core gas, while the internal regions have already been swept away (Fig. 1a and 1c). We have depicted this scenario in a sketch in Fig. 1d. The relatively low velocities of SO with respect to the systemic velocity, around ±10 km s$^{-1}$, and the fact that the gas in the outflow cavities appears redshifted on one side of the cavity and blueshifted on the other side (compare Fig. 1a and the sketch in Fig. 1d), suggest that the bipolar outflow is close to the plane of the sky.

### 3.1.2 *Spatial distribution and kinematics of P-bearing species: PN and PO*

The spatial distribution of the PN(2−1) emission is shown in the right panel of Fig. 2, where three different velocity ranges ([-6.5,-4.5], [-4.5,-2.0] and [-2.0, 0] km s$^{-1}$) are shown. For a direct comparison, we show the integrated maps of SO (left panel of Fig. 2) using the same velocity ranges. Unlike SO, PN(2−1) emission does not trace gas at high velocities. This is shown clearly in Fig. 3, where we compare the spatial distribution of PN with that of the high velocity gas traced by SO. There is a clear anticorrelation, i.e., the regions with high velocity gas traced by SO are devoid of PN emission.

The right panel of Fig. 2 shows that PN is distributed throughout the field peaking towards several visually-identified spots (P-spots, hereafter) located along the cavities of the bipolar outflow. We have identified seven P-spots in the PN map: P1 (in the northern outflow cavity), and P2 to P7 (in the southern cavity).

The spectra extracted in a circular region of 3″ diameter centered on the positions of the P-spots are shown in Fig. 4. PO is detected in the P3, P4 and P5/P6/P7 regions, and tentatively in the P2 spot. In Fig. 5 we show a zoom-in view for those P-spots for which clear PO emission has been detected. The emission of PN, PO and SO are spatially coincident in the P3 and P4 spots. In the case of the P5/P6/P7 spots, the PO spatial distribution is more similar to that of SO than to that of PN. P-bearing molecules and SO have not been detected towards the position of the starless core (SC).

We have also extracted spectra towards three additional positions in the region: the central MM position, and the peaks of the redshifted and blueshifted outflow lobes traced by the high velocity SO emission (HV-r and HV-b, respectively, hereafter; see Fig. 3). The coordinates of all the positions are indicated in Table 2. PN is barely detected in the surroundings of the MM position. PO is not detected at any of these positions. None of the P-bearing species is detected toward the HV-r and HV-b. The rightmost panel of Fig. 4 also shows the spectral profile of the SO $2_3-1_2$ transition. It is detected towards all the regions, being strongest at the MM position. The SO spectral profiles show several velocity components in some of the regions. In Section 3.1.3 we will analyze the spectra towards the different positions to derive the linewidths, velocities and column densities of the different species.

### 3.1.3 *LTE analysis*

We have analysed the spectra of PN, PO and SO extracted towards the different positions using two complementary analyses. In the first case, we have assumed Local Thermodynamic Equilibrium

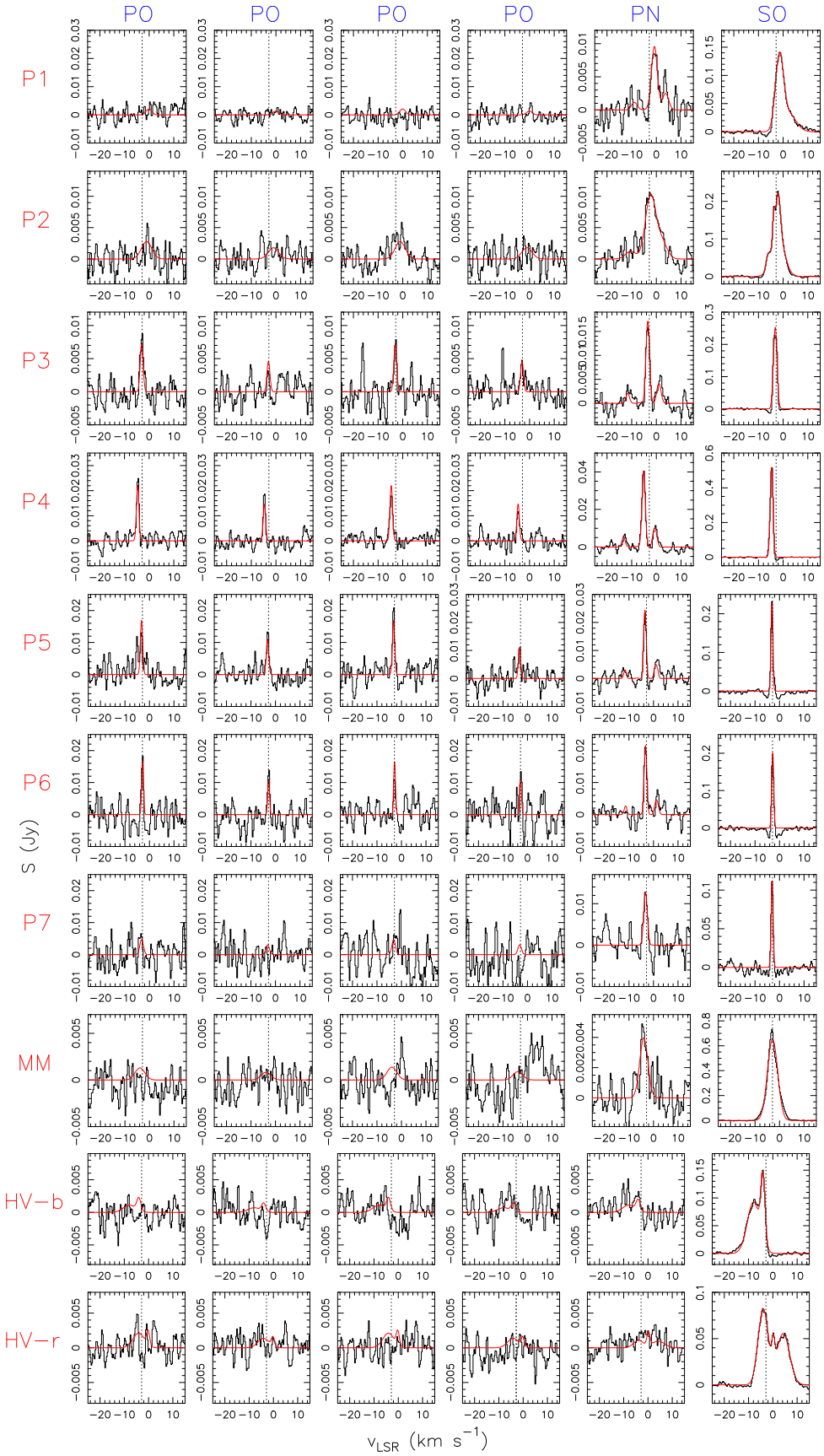


**Figure 4.** ALMA spectra of PO, PN and SO (molecular transitions listed in Table 1) towards different positions of the AFGL 5142 star-forming region, indicated to the left of the panels. The dashed vertical lines indicate the systemic velocity of the central core, -2.85 km s$^{-1}$. The red lines are LTE fits to the data obtained as explained in the text.

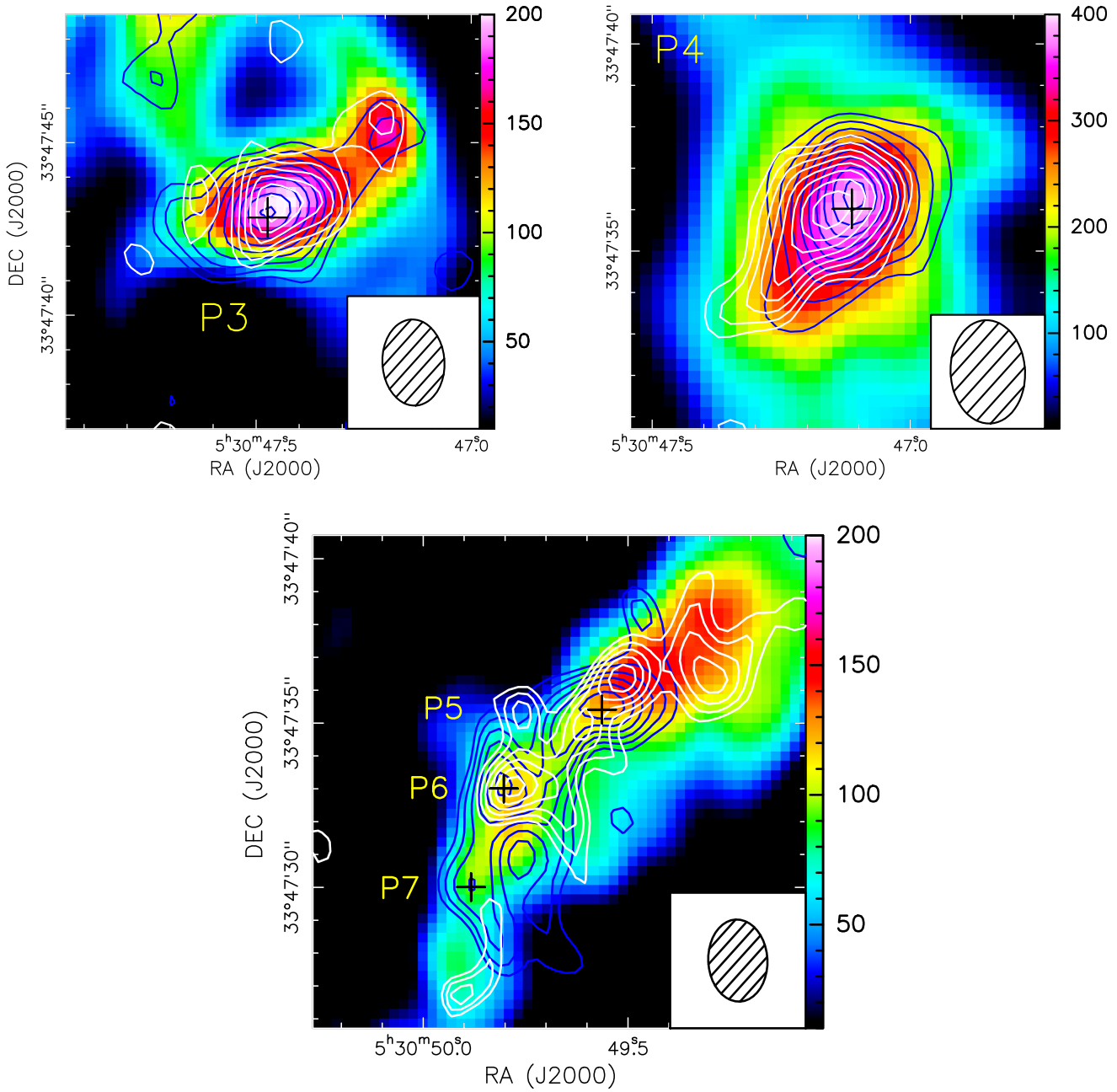


**Figure 5.** Zoom-in view of the P3 spot (upper left panel), P4 spot (upper right panel) and P5, P6 and P7 spots (lower panel). The color scale represents the integrated emission of the SO $2_3-1_2$ transition, in mJy beam$^{-1}$ km s$^{-1}$. The blue contours indicate the total integrated emission of the PN(2−1) transitions at 93.978209, 93.978477 and 93.97978 GHz. The contour levels start at 20/6/13 mJy km s$^{-1}$ beam$^{-1}$ and increase in steps of 5/3/3 mJy km s$^{-1}$ beam$^{-1}$ for the P3/P4/P5-P6-P7 regions, respectively. The white contours correspond to the combined integrated emission of the four hyperfine PO transitions (see Table 1). The contour levels start at 20/6/20 mJy km s$^{-1}$ beam$^{-1}$ and increase in steps of 5/3/5 mJy km s$^{-1}$ beam$^{-1}$ for the P3/P4/P5-P6-P7 regions, respectively. The positions of the different P-spots (Table 2) are indicated with black plus signs.

conditions (LTE), as we did in previous studies (Fontani et al. 2016; Rivilla et al. 2016, 2018; Mininni et al. 2018). We have used the Spectral Line Identification and Modeling (SLIM) tool of MADCUBA, which produces synthetic spectra of the molecules using the information from the publicly available spectral catalogs. For the analysis in this work, we have used the entries from the CDMS catalog (Müller et al. 2001, 2005). For PN our observations fully resolve for the first time the $^{14}$N hyperfine splitting (see Fig. 4)[4]. For this reason we have used the CDMS entry considering the $^{14}$N hyperfine splitting, and the partition function that considers the spin-multiplicities.

To derive the physical conditions, we have used the

[4] The hyperfine structure of PN(2-1) was marginally resolved in single-dish spectra of AFGL 5142 by Fontani et al. (2016) (see their fig. 1).

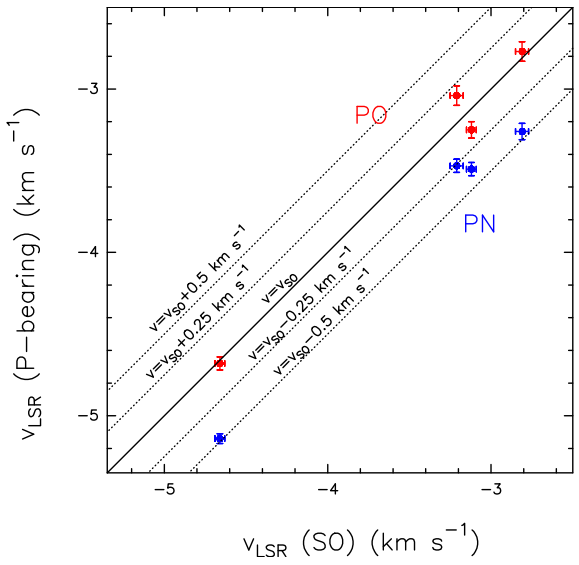


**Figure 6.** Velocity of PN (blue points) and PO (red points) as a function of SO velocity towards the P-spots for which the three species have been detected and the velocity was left as a free parameter in the AUTOFIT analysis: P3, P4, P5 and P6 spots, located in the southern (blueshifted) outflow cavity. The solid black line denotes equal velocities, and the dashed lines show differences of ±0.25 and ±0.5 km s$^{-1}$.

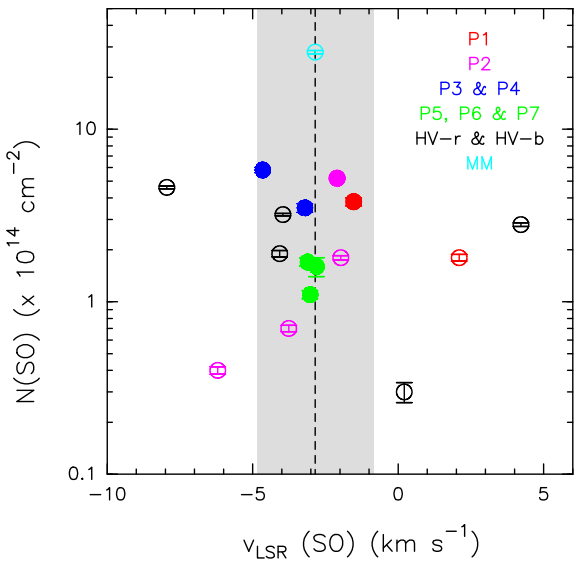


**Figure 7.** SO column density versus SO velocity towards the different positions in the AFGL5142 field studied in this work. The filled/empty circles indicates detections/non-detections of PN. The different colors denote different group of positions, as labeled in the upper right corner. The uncertainties on the column densities are indicated with error bars. The uncertainties on the velocities are within the size of the symbols. The systemic velocity of the central core, −2.85 km s$^{-1}$, is indicated with a vertical dashed line. The gray band indicates a velocity range of ±2 km s$^{-1}$ with respect to the systemic velocity, which contains all the regions with PN detections.

MADCUBA-AUTOFIT tool that compares the observed spectra with the LTE synthetic spectra of the different species, taking into account all transitions considered. This tool provides the best non-linear least-squared fit using the Levenberg-Marquardt algorithm. The free parameters are: total column density ($N$), excitation temperature ($T_{\rm ex}$), velocity ($v$), and full width at half maximum ($FWHM$). MADCUBA-AUTOFIT calculates consistently from these parameters the line opacity of each transition (see Rivilla et al. 2019). Since our data contain only a single rotational transition of the three species (PN, PO and SO), the excitation temperature cannot be derived, and hence we assumed fixed values. For the P-bearing species, we used the value found by Mininni et al. (2018) in this region using several transitions of PN, namely $T_{\rm ex}$=5 K. We note that the column densities of PN and PO can vary by a factor of 2.5 and 2.1, respectively, assuming different values of $T_{\rm ex}$ in the range of 5−50 K (lower column for higher temperatures). For SO, for which an earlier estimate of $T_{\rm ex}$ is not available, we used the kinetic temperature derived from observations of $NH_3$ (Busquet et al. 2011) of 34 K. The SO column density can vary by a factor of 1.4 assuming a different $T_{\rm ex}$ in the range of 10−50 K. Then, fixing $T_{\rm ex}$, we run MADCUBA-AUTOFIT leaving $N$, $v$, and $FWHM$ as free parameters. Towards some positions (e.g., P1, P2, HV-r and HV-b), we have used several velocity components to reproduce the profile of SO, fixing the value of the velocity as well. When the algorithm did not converge, we fixed manually the velocities and/or the FWHM to the values that best reproduced the observed spectra, and reran AUTOFIT. The results of the best fits are plotted in Fig. 4 and the derived physical parameters are shown in Table 3. The errors of the free parameters are derived from the diagonal elements of the covariance matrix, the inverse of the Hessian Matrix, and the final $\chi^2$ of the fit.

In the following, we summarize the main results of the analysis:

• The velocities of PN and PO are different. In the four P-spots for which the two species have been detected and the velocity was left as a free parameter (P3, P4, P5 and P6, all located in the southern blueshifted cavity) the differences are 0.4±0.1, 0.46±0.07, 0.24±0.09 and 0.5±0.1 km s$^{-1}$, respectively. Fig. 6 shows that the velocities of PN are lower than those of PO, namely PN is blueshifted with respect to PO. The velocities of PO are more similar to those of SO.

• Most of the P-spots have narrow linewidths in the range 0.9−1.7 km s$^{-1}$ (P3, P4, P5, P6 and P7), with the exception of P2, which has broader linewidths of 5−6 km s$^{-1}$. The narrow linewidths allowed us to fully resolve for the first time the $^{14}$N hyperfine structure of PN towards the P3 and P4 spots (Fig. 4). The quite narrow linewidths of PN and PO towards several P-spots, with values of 1−2 km s$^{-1}$, suggest that these molecular species might arise from post-shocked material, where turbulence has been already partially dissipated, rather than directly shocked material. A second alternative would be slow shocks due to the outflow *wind*, whose velocity can be significantly reduced compared to the one of the outflow axis, as observed.

• The derived line opacities of PN, PO and SO (see Table 3) are low ($\tau$ <0.1) in most of the positions. Only at P4 the transitions are slightly more optically thick, with $\tau$ ∼0.2 (for PN and SO), while towards the central MM position the opacity of SO is $\tau$ =0.278±0.009.

• In the positions where the two P-bearing molecules have been detected, the molecular abundance ratio PO/PN is always larger than 1, with the only exception of the P-spot located closer to the protostar, P2, where the ratio is 0.6±0.2. In the other P-spots the ratio spans from 1.4 to 2.6 (Table 4). This confirms previous findings from IRAM 30m single-dish observations in the W51 and W3(OH) massive star-forming regions (Rivilla et al. 2016), the protostellar shock L1157 (Lefloch et al. 2016), and the Galactic Center G+0.693 cloud (Rivilla et al. 2018), where the PO/PN ratio ranges from 1.8 to 3.

• The abundance SO/PN ratio spans from 70 to 207 in the

**Table 5.** Results of the non-LTE analysis of PN and PO towards the P-spots where both species have been detected. The column densities have been obtained assuming $T_{kin}$=20 K and three different gas densities $n$ ($10^4$, $10^5$ and $10^6$ cm$^{-3}$).

| Region | $N$(PN) ($10^{12}$ cm$^{-2}$) | | | $N$(PO) ($10^{12}$ cm$^{-2}$) | | | [PO/PN]$_{non-LTE}$ | | |
|---|---|---|---|---|---|---|---|---|---|
| | $n$=$10^4$ | $n$=$10^5$ | $n$=$10^6$ | $n$=$10^4$ | $n$=$10^5$ | $n$=$10^6$ | $n$=$10^4$ | $n$=$10^5$ | $n$=$10^6$ |
| P2 | 26.9 | 4.5 | 4.0 | 39.0 | 8.0 | 9.0 | 1.4 | 1.8 | 2.2 |
| P3 | 14.7 | 2.4 | 2.0 | 39 | 8 | 9 | 2.7 | 3.3 | 4.5 |
| P4 | 44 | 5.7 | 4.6 | 113 | 21 | 21 | 3.1 | 4.4 | 5.5 |
| P5 | 17.0 | 2.5 | 2.1 | 82 | 16 | 16 | 4.8 | 6.4 | 7.6 |
| P6 | 16.1 | 2.4 | 2.0 | 57 | 11 | 12 | 3.5 | 4.6 | 6.0 |

P-spots. These values are orders of magnitude lower than the one at the MM position, which is 3365, and those towards HV-r and HV-b, which are >1000 (Table 4). The SO column densities towards these regions are not affected by optical depth effects, since the opacities derived from our analysis are ≤0.3 (Table 3). In any case, we note that even in the case of optically thick conditions, the SO column densities would be lower limits, and thus also the SO/PN value would be a lower limit. Therefore, the SO/PN values found in the P-spots are significantly lower than those of other regions with strong SO emission. Comparison between the low value of the SO/PN ratio found in the P-spots and those of the central MM position demonstrates that, while SO traces not only the outflow cavities but also the central core surrounding the protostar (indeed SO peaks towards the MM position), PN emission traces only the cavities. This suggests that P-bearing molecules are excellent tracers of outflow cavity walls. The SO/PO ratio, shown in the last column of Table 4, ranges between 27 and 309 in the P-spots, while it is > 4500 at the MM position.

• As previously mentioned, PN and PO are only detected at velocities relatively close to the systemic velocity of the core (± 2 km s$^{-1}$), while SO traces also gas at high velocities (Fig. 3), as can be seen in the spectra towards P1, P2, HV-r and HV-b (Fig. 4). To study this in more detail, we compare in Fig. 7 the column density versus the velocity of SO in the regions considered in this work: the P-spots, MM, HV-r and HV-b positions. The P-spots have SO column densities in the range ∼(1−10)×$10^{14}$ cm$^{-2}$, and SO velocities ranging from ∼ −5 to −1 km s$^{-1}$. Other regions with comparable SO column densities, but higher velocities with respect to the systemic velocity, do not exhibit emission from P-bearing species. These regions include the HV-r and HV-b positions, and also additional velocity components of the P-spots in which emission of P-bearing species is not detected (Table 3). Therefore, the non-detection of P-bearing species in the high-velocity SO spots is not due to a lower column density of SO.

#### *3.1.4 Non-LTE analysis*

Previous works have assumed LTE conditions to estimate column densities of PN (Ziurys 1987; Yamaguchi et al. 2011; Fontani et al. 2016; Mininni et al. 2018; Rivilla et al. 2018) and PO (Rivilla et al. 2016; Lefloch et al. 2016; Rivilla et al. 2018). However, this assumption may not hold, because the gas densities in the observed regions may not be high enough for the collisional excitation of the lines to compete with radiative decay, and to maintain a Boltzmann distribution of the energy levels. To test the LTE assumption for the mm-wave lines of PN and PO, we used the non-LTE radiative transfer program RADEX[5] (Van der Tak et al. 2007). This program solves for the radiative and collisional (de)excitation of the molecular energy levels, and treats optical depth effects with an escape probability formalism. For PN, we implemented in RADEX the collisional coefficients from Toboła et al. (2007). For PO, we used the cross-sections derived by Lique et al. (2018) to calculate the collisional rates, which are presented in Appendix B.

The collisional data for the PN-He system (Toboła et al. 2007) were scaled by 1.385 to account for $H_2$ as the dominant collision partner. These data cover the lowest 31 rotational levels of PN, up to 723 cm$^{-1}$ for temperatures between 10 and 300 K. For PO, the recent collision data with He (described in Appendix B) were scaled by 1.4 to mimic $H_2$. These data cover the lowest 116 rotational hyperfine levels of PO, up to 296 cm$^{-1}$ for temperatures between 10 and 150 K. Both datafiles are available on the LAMDA[6] database (Schöier et al. 2005).

To study the excitation conditions of the P-bearing molecules as a function of the volume density of the gas, we have run RADEX assuming three different values: $n(H_2)$ = 1×$10^4$, 1×$10^5$ and 1×$10^6$ cm$^{-3}$. The calculations assume a kinetic temperature of $T_{kin}$ = 20 K and a background temperature of 2.73 K. For each volume density, we have then derived the column density that produces the observed line fluxes (in units of K km s$^{-1}$) of the PN $J$=2–1 and the PO J=5/2−3/2, Ω=1/2, F=3−2, l=e transitions towards the P-spots where both species are clearly detected. The results are shown in Table 5. The derived column densities increase for densities $n(H_2)$ = 1×$10^5$ and especially $n(H_2)$ = 1×$10^4$ cm$^{-3}$ due to strong sub-thermal excitation effects. We also show in Table 5 the PO/PN ratio derived at the different densities. Lower gas densities produce lower ratios, but in all cases PO/PN is >1, reaching values up to 7.5 in the P5 spot.

### 3.2 ROSINA measurements of the comet 67P/C-G

Altwegg et al. (2016) reported the detection of a clear signal on mass 31 Da attributable to P in the comet 67P/C-G using ROSINA data, although it was not possible to detect the parent molecule(s) at that time due to mass line interferences. A re-evaluation of the data has now given more insight into the chemistry of P. The only time when there was a clear detection of atomic P on mass 30.9737 Da was when *Rosetta* orbited in the terminator plane at 10 km from the nucleus centre from October 14 to October 29 2014. Before and after this time, *Rosetta* was too far from the comet and/or the production rate was too low. A full orbit around the comet took ∼2.5 Earth days, which means 5 full orbits for the whole period. ROSINA obtained ∼1 spectrum/hour for ∼20h/day for the full mass range. So the number of spectra is on the order of 200 spectra per mass. In about 1/3 of them P could be detected in a statistically significant

[5] https://personal.sron.nl/~vdtak/radex/index.shtml

[6] http://home.strw.leidenuniv.nl/~moldata/

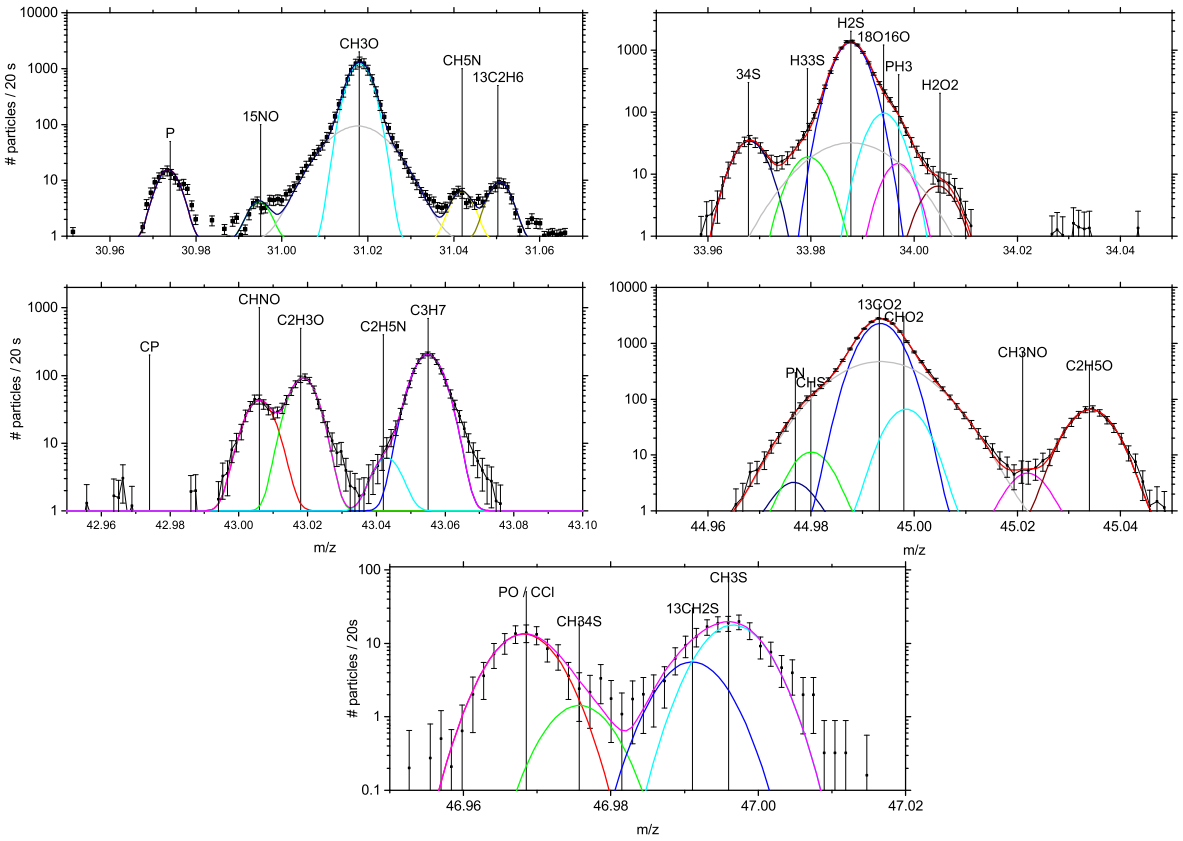


**Figure 8.** ROSINA DFMS mass spectra for masses 30.9737 Da (P), 46.9681 Da (PO), 33.9967 Da ($PH_3$), 42.9732 Da (CP) and 44.9763 Da (PN). The integration time is 20 s per spectrum. Error bars represent $1\sigma$ counting statistics. The colored curves correspond to the fit of different species .The P peak was already identified by Altwegg et al. (2016). Regarding the P-bearing molecules, only PO shows a distinct peak at the correct location (see text for the discussion of possible contribution from CCl). For $PH_3$, there is a strong overlap with $^{18}O^{16}O$ and with abundant $H_2S$. PN has an overlap with CHS, and CP cannot be detected.

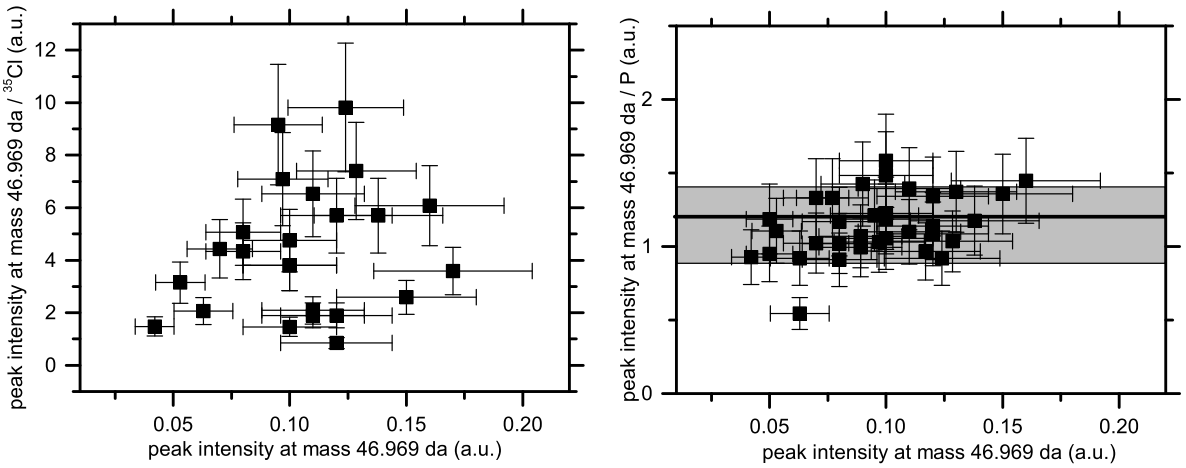


**Figure 9.** Correlation plots between the peak at mass 46.696 Da and $^{35}Cl$ (left panel) and P (right panel) as a function of the peak intensity, from ROSINA measurements of the comet 67P/C-G. In the right panel, the black solid line indicates the mean value of the different points, and the grey area denotes the uncertainty of this mean.

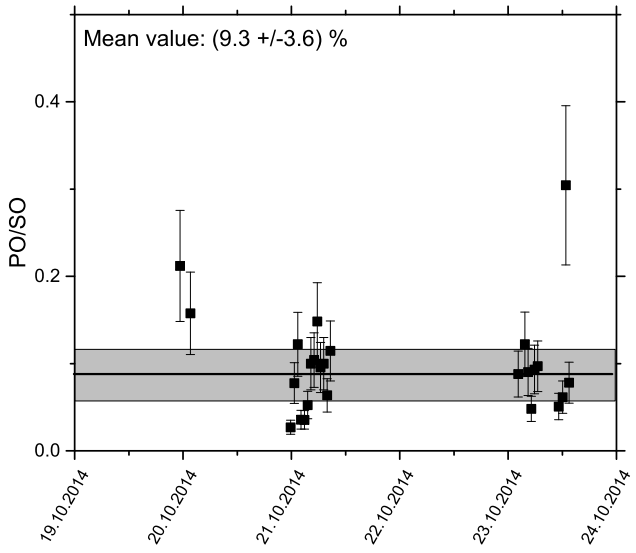


**Figure 10.** Ratio of PO/SO count rates as a function of time from ROSINA measurements of the comet 67P/C-G. The black solid line indicate the mean value of the different points, and the grey area denotes the uncertainty of this mean.

amount due to the large diurnal and seasonal density variations. To look for possible parents of P, beyond mass 31 Da, we have also analysed masses 34 Da for $PH_3$, 43 Da for CP, 45 Da for PN, 47 Da for PO. Sample spectra for 31, 34, 43, 45, and 47 Da are given in Fig. 8.

The P peak on mass 31 Da is easy to detect, as it is separated from other contributions on mass 31 Da. $PH_3$ is completely hidden beneath the peaks of $^{18}O^{16}O$ and abundant $H_2S$. No signal could be detected at the mass of CP, which would be well separated from interfering peaks. PN is completely hidden by the peaks of CHS and $^{13}CO_2$.

At the mass of PO (46.696 Da), there is a clear peak. However, PO and CCl strongly overlap because their masses are identical up to the fourth digit. In order to see if the peak at 46.969 Da is due to CCl or PO or both, we checked the correlation of the ratio of this peak with the P peak on mass 31 Da and with the $^{35}Cl$ peak on mass 35 Da. The result is shown in Fig. 9. The ratio $m_{46.696}$ / $^{35}Cl$ or $m_{46.696}$ / P, respectively, should be nearly constant whether the peak on mass 46.696 Da is due to CCl or PO, respectively. This is the case for P, but not for $^{35}Cl$. A possible parent of CCl could be $CH_3Cl$. According to NIST (Stein 2016), the fragment CCl from $CH_3Cl$ is about 7% of the parent molecule. This would mean that the signal for $CH_3Cl$ should be well above 100 particles / 20 s. No signal at all was detected on mass 50 Da of $CH_3Cl$, although later in the mission there is clear evidence for $CH_3Cl$ (Fayolle et al. 2017). $CH_3Cl$ seems to be correlated to dust which was not abundant in October 14. We therefore exclude the presence of CCl and attribute all of the peak at mass 46.696 Da to PO.

In order to derive a relative abundance of PO, we have to make a few assumptions: i) we assume that the ionization cross section of PO is the same as for NO as there exist no data for PO and it cannot easily be calibrated in the lab due to its unstable and possibly poisonous nature; ii) we assume the same instrument sensitivity for SO and PO as they are very similar in mass, which cancels out the mass dependent sensitivity of the instrument.

Fig. 10 shows the correlation between PO and SO. In order to get the quantity of SO we also have to take into account $SO_2$ and then subtract the fragments from $SO_2$ from the signal on SO (for details see Calmonte et al. 2016). SO and PO correlate well. These measurements were done at 3 au inbound, when there was a large heterogeneity in the coma between $CO_2$, CO and $H_2O$ (Hässig et al. 2015), depending on the sub-spacecraft latitude. SO behaves similar to CO as does PO. A correlation with, e.g., water or methanol, yields huge spreads. The good correlation between SO and PO suggests that they are embedded in a similar way in the ice and have similar sublimation temperatures, which depend mostly on the matrix in which they are embedded.

For other P-bearing molecules, we can only get upper limits. We assume that the ionization cross sections of all the species are similar. The signal on mass 45 Da gives an abundance ratio of PO/PN>10. An abundance ratio of PO/$PH_3$ >3.3 would still be compatible with our mass spectra and a Solar $^{18}O$ / $^{16}O$ ratio. There is no signal for CP, which means a ratio of PO/CP >33.

The signal at mass 31 Da is a daughter product of PO and possibly $PH_3$. Taking the fragmentation pattern of $NH_3$ as a proxy for $PH_3$, only very little P is produced. That means that most of the peak at mass 31 Da has to be attributed to PO which adds to ~70%. To reach this conclusion, we have taken the mass dependent sensitivity of DFMS into account. This yields, finally, an abundance of PO relative to SO of 16% with a probable uncertainty of a factor of 2 due to the assumptions made. This implies a SO/PO ratio of ~6.

While PO was not detected later in the mission, SO is present throughout, due to its higher abundance. Calmonte et al. (2016) have deduced a nucleus bulk abundance for SO/$H_2O$ of $7\times10^{-4}$ for the period May/June 2015 just before perihelion, but outside of the dust outbursts of the near perihelion phase (Vincent et al. 2016). If we assume that PO and SO are indeed well correlated, this would yield a relative abundance for PO/$H_2O$ of $1.1\times10^{-4}$ for the nucleus bulk within a factor of 2.

The P/O ratio found in the comet is $0.5-2.7\times10^{-4}$, close to the Solar value of $5.8\times10^{-4}$, indicating that P is only slightly depleted (see also Rubin et al. 2019).

## 4 DISCUSSION

### 4.1 Formation of P-bearing molecules in star-forming regions: the role of shocks and photochemistry

#### *4.1.1 Hints from the spatial distribution of the emission*

We have presented the first high-angular resolution maps of P-bearing species (PO and PN) in a star-forming region, which allow us to shed light on the poorly constrained chemistry of interstellar P. The non-detection of strong emission of P-bearing species towards the positions of the central hot core (MM position) and the position of the starless core (SC) seems to challenge the formation theories based on hot gas-phase chemistry triggered by the warm-up of protostars (Charnley & Millar 1994), and on cold gas-phase chemistry during the prestellar collapse phase of the parental core (Rivilla et al. 2016).

Previous theoretical models (Aota & Aikawa 2012; Jiménez-Serra et al. 2018) propose that shocks are the most important agent for the chemistry of P-bearing species. According to this scenario, the ice mantles of the grains are sputtered due to the mechanical

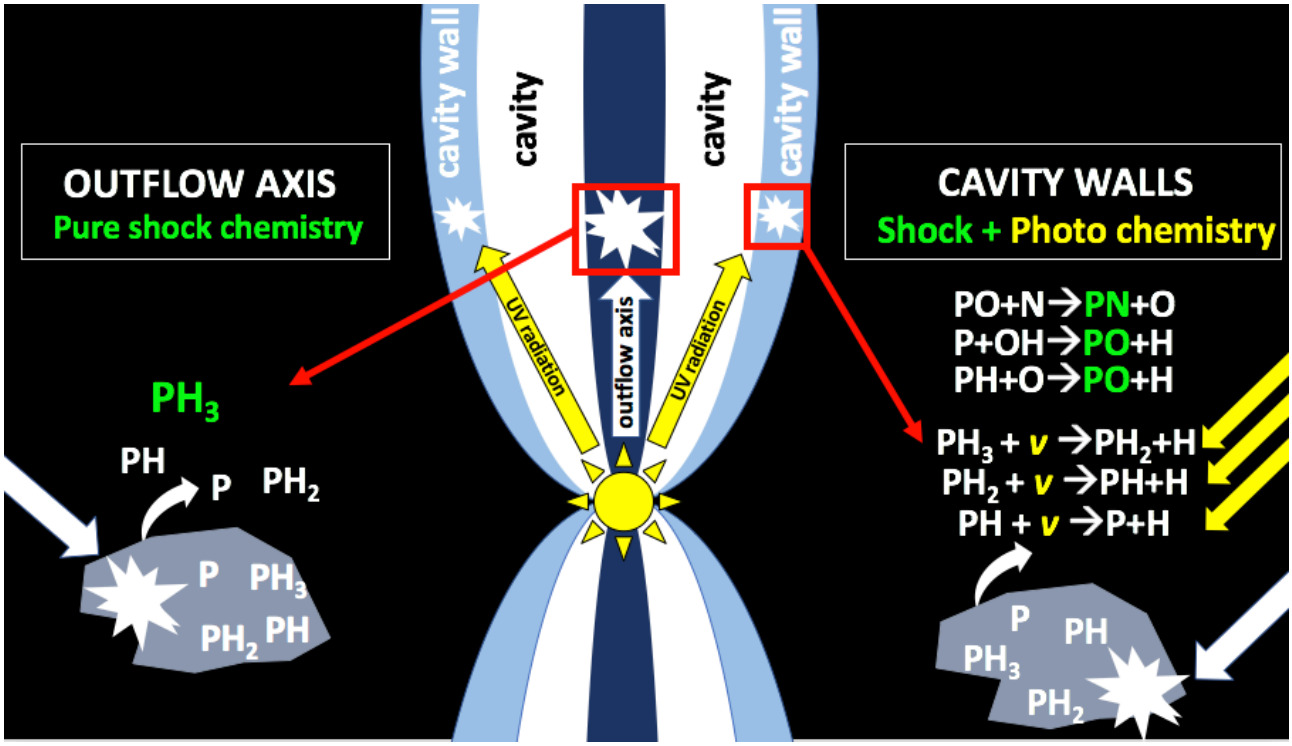


**Figure 11.** Scenario proposed for the formation of P-bearing species in the cavity walls excavated by a molecular outflow. Along the high-velocity outflow axis, the chemistry is mainly dominated by shocks, and $PH_3$ is expected to be the most abundant P-bearing species. In the UV illuminated cavity walls, photochemistry is producing PO and PN.

energy of the shocks, releasing P into the gas phase. The shock scenario has been supported by the detection of PN and PO in a protostelar shock (Lefloch et al. 2016) and by the observations of Rivilla et al. (2018) in a survey of molecular clouds in the center of our Galaxy. In this study, we found that PN and PO are only detected in the regions whose chemistry is dominated by large-scale shocks, and the abundances of PN correlate with those of the typical shock tracer SiO (e.g., Martin-Pintado et al. 1992). This observational correlation between PN and SiO has also been confirmed in a survey of high-mass star-forming regions observed with single-dish telescopes (Mininni et al. 2018, Fontani et al., submitted), suggesting a link between shocks and the presence of P-bearing species.

However, our high-resolution ALMA observations towards AFGL 5142 have provide us with essential new information that challenges the idea that shocks are the *main* driver of P-chemistry. PN and PO have been found only in the cavity walls (Fig. 2), and not along the central high-velocity parts of the bipolar outflow (e.g., HV-r and HV-b positions), where SO is also prominent (Figs. 3 and 7). This indicates that the mere presence of shocked material does not guarantee the detection of PO and PN. This may suggest that these molecules are not directly sputtered from grains, but are likely formed later through gas-phase chemistry.

Jiménez-Serra et al. (2018) studied the chemistry of P-bearing species theoretically, considering not only the presence of protostellar shocks, but also other physical mechanisms such as protostellar heating, UV and cosmic-ray irradiation. Based on our ALMA maps of AFGL 5142 and the predictions of these chemical models, we propose that, besides shocks, photochemistry is also key for regulating the abundance of P-bearing species. We depict this scenario in the scheme presented in Fig. 11. Along the outflow axis, traced by the high-velocity SO emission, the chemistry is mainly dominated by shocks. In this region, atomic P on the surface of dust grains is efficiently hydrogenated forming species such as PH, $PH_2$ and mainly $PH_3$, which afterwards desorb thanks to shock-induced grain sputtering. This region of high-velocity gas is thought to be younger than the material of the cavity walls, and further gas-phase chemistry is thus not expected because it would need longer timescales. In this scenario, $PH_3$ should be the dominant P-bearing species in the freshly desorbed material, according to the shock model of Jiménez-Serra et al. (2018). Since the extinction is higher along the outflow axis than in the direction of the cavity walls, the UV photons are not efficient converting $PH_3$ to PO and PN through gas-phase photochemistry.

In contrast, the situation in the cavity walls is different. Since they are more exposed to the UV photons arising from the central protostar, photochemistry can govern the chemistry. As indicated in Fig. 11, the hydrogenated P-bearing species desorbed by shocks (e.g. $PH_3$) can rapidly (on short timescales of $10^{4-5}$ yr) be converted to PO and PN, according to the gas-phase photochemistry models of Jiménez-Serra et al. (2018). The formation of PO and PN is enhanced in the cavity walls, where the volume densities become large enough for formation reactions to proceed rapidly. Thus, the scenario depicted in Fig. 11, with a combination of shocks and photochemistry, may explain why PO and PN are only observed in the cavity walls and not along the outflow axis. A positive detection

of $PH_3$ in the shocked gas along the outflow axis would support this hypothesis.

It should be noted that photochemistry might be not only productive (converting $PH_3$ into PO and PN), but also destructive. Assuming a UV radiation field of 10 $G_0$, and using the photodestruction rates proposed by Jiménez-Serra et al. (2018), $3\times10^{-10}$ $s^{-1}$ and $5\times10^{-12}$ $s^{-1}$ for PO and PN, respectively, the unshielded timescales for visual extinctions $A_V$ >5 mag[7] are $>2\times10^5$yr and $>4\times10^{10}$yr, respectively. So, in principle, P-bearing molecules (including PO that is more easily photodissociated) can survive for relatively long times if they are partially shielded, in agreement with our observations.

#### 4.1.2 *Hints from molecular abundance ratios*

The observed PO/PN molecular abundance ratios are a key additional constraint that supports this scenario. We have found that PO is more abundant than PN towards most of the P-spots, with the only exception of P2. Previous detections in star-forming regions and the Galactic Center cloud G+0.693 (Rivilla et al. 2016; Lefloch et al. 2016; Rivilla et al. 2018; Bergner et al. 2019) found also that the PO/PN ratio is ≥ 1. However, these values > 1 are never produced by the pure shock models of Jiménez-Serra et al. (2018) (see their Fig. 11). To reproduce the observed PO/PN ratios, these authors offer several alternatives. The first one is hot chemistry (∼100 K) produced by protostellar heating. However, our ALMA observations did not detect P-bearing emission in the central hot core-like region surrounding the central protostar, but in the colder cavity walls, ruling out this possibility.

A second possibility proposed by Jiménez-Serra et al. (2018) is a high cosmic-ray ionization rate. Enhanced values of the cosmic-ray ionization rate with respect the typical interstellar values ($\zeta$=$10^{-17}$–$10^{-16}$ $s^{-1}$, Indriolo et al. 2015), have been claimed in molecular outflows powered by low- and intermediate-mass stars (Ceccarelli et al. 2014; Podio et al. 2014), with values of $\zeta$ spanning from ∼$10^{-12}$ to $10^{-16}$ $s^{-1}$, and in protocluster star-forming regions like OMC–2 FIR4 ($\zeta$ ∼$10^{-14}$; Fontani et al. 2017). One may expect a similar effect in a massive star-forming region such as AFGL 5142. These high values might be reached due to the acceleration of both cosmic-ray protons and electrons through diffusive shock acceleration (Padovani et al. 2016). However, a high cosmic-ray ionisation rate is unlikely to be the reason of the PO/PN ratios observed. First, because the models by Jiménez-Serra et al. (2018) that predict PO/PN∼10 does not only need $\zeta$=$1.3\times10^{-13}$ $s^{-1}$, but also high temperatures ∼100 K, which are not present in the AFGL 5142 outflow cavities. Second, while is true that the combination of high $\zeta$ and high temperature produce high PO/PN ratios, the absolute molecular abundances are very low, ≤$10^{-12}$ (see Fig. 6 of Jiménez-Serra et al. 2018), which are below the detection limits. And third, the mechanism proposed by Padovani et al. (2016) to increase the cosmic-ray ionisation rate is expected to be mainly relevant along the outflow axis rather than in the cavity walls.

The last alternative to produce high PO/PN ratios is photochemistry. As shown in Fig. 11 of Jiménez-Serra et al. (2018), the models based on photochemistry with intermediate extinctions ($A_V$ ∼7 mag) produce PO/PN>1, as observed in the cavity walls of AFGL 5142. This is further support for the photochemistry scenario we are proposing. Moreover, we have seen before that PO is easier to photodissociate because it is thought to have a larger photodestruction rate than PN by almost 2 orders of magnitude (Jiménez-Serra et al. 2018). Therefore, PO is expected to be more efficiently destroyed close to the star, where the UV radiation is more intense. Moreover, even if PN is photodissociated, it may be able to reform again (unlike PO) thanks to the large amounts of atomic P available in the gas phase, which react via P + CN → PN + C (Jiménez-Serra et al. 2018). Consequently, the PO/PN ratio is expected to increase with decreasing UV flux, i.e., with increasing distance from the protostar. This theoretical prediction can be checked using our ALMA data. In Fig. 12 we show that the PO/PN ratio in the different P-spots of the southern cavity walls of AFGL 5142 (normalized to the ratio found in the P-spot P2), obtained by the LTE and non-LTE analyses. In all cases, the PO/PN ratio clearly increases with increasing distance from the central protostar, supporting the role of photochemistry to explain the observed relative abundances of PN and PO. We note however that a proper physical modeling of the source coupled with a detailed treatment of photochemistry should be done in the future to fully confirm this scenario proposed here qualitatively.

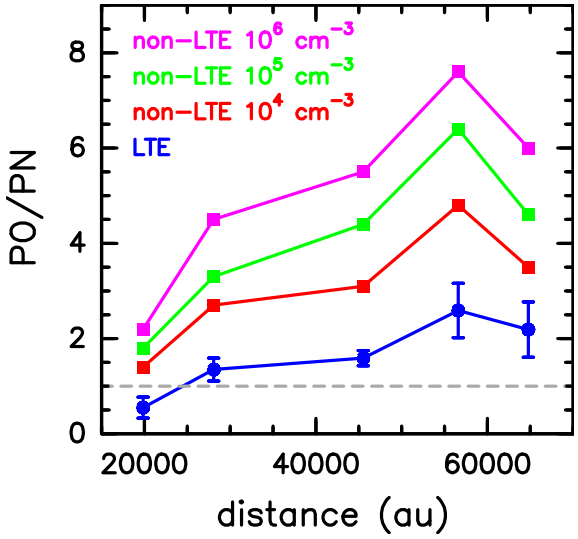


**Figure 12.** PO/PN molecular ratio, normalized to the ratio found in the P2 spot, as a function of the distance to the central MM position. We have included all the P-spots of the southern cavity, with the exception of the P7 spot, because it is located very close to the primary beam of the observations, where poorer sensitivity may affect the accuracy of the measured PO column density. The different colors indicate the molecular ratios obtained with the LTE approximation (blue dots) and the non-LTE analysis considering different densities: $10^4$ $cm^{-3}$ (red squares), $10^5$ $cm^{-3}$ (green squares), and $10^6$ $cm^{-3}$ (magenta squares).

#### 4.1.3 *Scenario proposed for the formation of PO and PN*

In summary, the scenario that emerges from our ALMA observations of AFGL 5142 explains the formation of P-bearing species in three main phases:

- Rapid hydrogenation of atomic P on the surface of dust grains, which form efficiently $PH_3$ during the early cold phase.
- Grain disruption induced by protostellar outflows that desorb $PH_3$ into the gas phase.
- Destruction of $PH_3$ and formation of PO and PN through gas-

[7] The UV radiation field is attenuated due to the visual extinction $A_V$ following the exponential decay $e^{-\gamma A_V}$. We have used $\gamma$ of 2 and 3 for PO and PN, respectively, as proposed by Jiménez-Serra et al. (2018).

phase photochemistry in the outflow cavity walls, which are exposed to significant UV radiation from the central protostar.

Therefore, we propose that PO and PN are formed after the protostellar birth, since they are a consequence of events produced by the protostellar activity: shocks and UV radiation. This scenario may be favoured in regions with high $H/H_2$ ratio, such as those dominated by photons, which are typical of high-mass star-forming regions like AFGL 5142.

According to the scenario summarized in Fig. 11, PO is formed via PH + O, and also via P + OH. This latter formation route, not yet included in any chemical database, has been recently proposed by Jiménez-Serra et al. (2018). Although theoretical calculations and laboratory experiments are needed to confirm the viability of this reaction, we have found observational evidence that supports it. Our ALMA data shows that while PN and PO are systematically shifted in velocity by ∼0.5 km $s^{-1}$ (being PN more blueshifted, Fig. 6), PO and SO share the same velocity in the different regions studied. Moreover, Fig. 5c shows that PO follows the morphology of SO better than PN. Therefore, the observational correlations (spatial and kinematical) between PO and SO in the P-spots support the proposed formation route P + OH → PO + H, since SO is formed in a similar way in the gas phase: S + OH → SO + H (Kaufman & Neufeld 1996; Laas & Caselli 2019).

The different velocities of PO and PN (Fig. 6) suggest that both species trace different layers of the outflow cavity walls, which may have slightly different physical conditions. Observations have shown than oxygen- and nitrogen-bearing species behave very different in relatively cold regions of the ISM, in particular they differ on how they deplete onto dust grains (e.g. Caselli et al. 2017). At low temperatures (below 20 K) O-bearing species deplete significantly, while N-bearing species do not show evidence of depletion or freeze-out (e.g. Hily-Blant et al. 2010; Spezzano et al. 2017). Therefore, in the gas PN would survive better than PO in the coldest layers of the outflow cavity walls, those located farther away with respect to the protostar. In constrast, the closest layers of the cavity wall, more exposed to the protostellar heating and then with slightly higher temperatures, would favor the presence of PO (and SO). This could explain the observed differences between the velocities of the O-bearing (PO and SO) and the N-bearing species (PN). We have seen that PN is more blueshifted than PO and SO in the P3, P4, P5 and P6 spots, which are located in the sourthern and blushifted cavity of the outflow. In an accelerating outflow, the higher velocity of PN with respect to the central position may indicate that PN is arising from a deeper (and thus colder) layer in the cavity walls, where O-bearing species are more depleted.

The angular resolution of our ALMA maps (∼2″) is likely not high enough to resolve spatially these different regions in the cavity walls. Fig. 5 does not show clear differences in the morphology of PO and PN towards the P3 and P4 spots. In the case of the P5/P6/P7 regions, as already mentioned, there is a difference in the spatial distribution of PO (that follows SO) and PN. The latter appears shifted towards the SE, i.e., farther from the protostar. As a consequence, this part of the cavity may be indeed colder than that traced by PO, in good agreement with the selective depletion scenario described before. However, the current data only allows to draw some speculative conclusions, and higher angular resolution observations are needed to test this hypothesis.

### 4.2 The chemical thread of Phosphorus

#### *4.2.1 From the ISM of star-forming regions to Solar-system bodies*

We have described in the previous section how PO and PN can be synthesized in the ISM. We have seen that a massive star-forming region such as AFGL 5142 is a environment favorable for the formation of these P-bearing species, since it provides the two main physical agents required: protostellar shocks to sputter P from the dust grains and UV photons to trigger the photochemistry that forms PO and PN. The question now is to understand how this P reservoir that is available in the gas phase of a massive star-forming region can be incorporated to a planetary system similar to our Solar System. In this sense, the comparison between the P-content of AFGL 5142 and that of the comet 67P/C-G can give us important clues.

It is well known that most stars are not born in isolation, but within clusters (e.g., Carpenter 2000, Lada & Lada 2003) that also include massive stars (e.g., Rivilla et al. 2013b,a, 2014). There is multiple and independent evidence that indicate that our Sun was not an exception. Based on the observed extreme orbital eccentricity of the minor planet Sedna and the measurements of short-lived radioactive species (e.g. $^{26}Al$) inferred from meteorites, it has been proposed that our Sun was born in a cluster with $10^3$–$10^4$ stellar members (Adams 2010, Pfalzner et al. 2015), including massive stars. As a consequence, the chemical content of the ISM of the natal (massive) star-forming region might be incorporated into the ProtoSolar Nebula (PSN) and into the Solar System bodies, including comets and our own planet.

The abundances of P-bearing molecules with respect to $H_2$ found in the AFGL 5142 star-forming region are difficult to estimate, since the abundance of $H_2$ in the P spots is unknown. Using the molecular abundances of P-bearing species reported in previous works of $10^{-9}$–$10^{-10}$ (Fontani et al. 2016; Rivilla et al. 2016; Lefloch et al. 2016; Mininni et al. 2018; Bergner et al. 2019), we infer that the P in these molecules account for the 0.03% - 0.3% of the cosmic P. This is certainly a small fraction of the total P content in the ISM, although non negligible. This P in the form of simple volatiles, if transferred during the star formation process to Solar System bodies, could be enough to provide a reservoir of P accessible for prebiotic chemistry, creating an environment favorable to foster Life (see further discussion in next section).

Thanks to the *Rosetta* mission, there is now multiple evidence indicating that the chemical composition of the comet 67P/C-G was set before the birth of the Sun, and has survived almost unaltered since then. Measurements of $N_2$ (Rubin et al. 2015), deuterated species (Altwegg et al. 2017a), $S_2$ (Calmonte et al. 2016), Xe (Marty et al. 2017), and $O_2$ (Bieler et al. 2015), among others, have shown that the ice composition of the comet is pre-Solar.

Similarly, our analysis of PO in 67P/C-G suggests that it was already in the ice in the prestellar phase. *In-situ* photochemistry can be ruled out as the origin of the observed PO, since it was detected at ∼10 km from the nucleus at 3 au. This means that the molecules are exposed to a (weak) Solar illumination during only ∼10s, so photochemistry cannot take place. The ROSINA data have been examined for larger, more complex P-bearing molecules (such as $PO_2$, $PO_3$, $H_xPO_y$), yielding negative results. Moreover, PO is suspected to be strongly correlated with $CO_2$, since it shows higher abundances over the southern (winter) hemisphere, similar to $CO_2$ and contrary to $H_2O$, which was more abundant in the north at that time. This suggests that PO is mixed with $CO_2$ ice. Hence, there is no evidence to suggest that PO stems solely from the surface of the comet, nor it being a fragment of some other P-rich compound.

Therefore, the volatile PO measured by ROSINA arises from ices that were assembled prior to the formation of the comet. This means that the comet may have directly inherited the chemical composition of its parental PSN, which was originated in a clustered environment with neighboring massive protostars.

We have shown in this work that PO is more abundant than PN in the massive star-forming region AFGL 5142, confirming previous results in other massive star-forming regions (W51 and W3(OH), Rivilla et al. 2016). Interestingly, the analysis of ROSINA data indicate that PO is also more abundant than PN in the comet 67P/C-G by a factor of >10. This predominance of PO with respect to PN in both cases is in agreement with the idea that the chemical composition of the comet was incorporated from the natal nebula.

The ROSINA data also confirm that PO is more abundant than $PH_3$ at least by a factor of 3.3. As explained in Sect. 4.1, the conversion of $PH_3$ to PO needs the action of photochemistry (see Fig. 11). Therefore, the ROSINA measurements suggest than the cometary ices suffered some UV processing prior to the formation of the comet, probably due to intense irradiation from neighboring massive stars.

Moreover, we have seen that PO and SO are well correlated in the ROSINA data (Fig. 10), indicating that they are similarly embedded in the cometary ice. In the cavity walls of AFGL 5142, both species are also correlated, spatially and kinematically, suggesting also a similar formation mechanism, as discussed in Section 4.1.

These similarities may indicate that the chemical composition of the comet, and in particular the PO budget, comes from a shocked (first) and UV-illuminated (afterwards) gas condensation of the massive star-forming cluster that formed the Solar System. In this condensation, after a sudden decrease of the temperature due an increase in density and efficient dust cooling, PO condensed on grains along with other molecules, including complex species also detected in the comet (Goesmann et al. 2015; Altwegg et al. 2017b). Under these physical conditions, deuteration increased, producing heavy water and other deuterated species detected in the comet (Altwegg et al. 2017a). PO does not react easily with atomic H, which is the only mobile species on the dust grains at low temperature. This allowed a relatively high abundance of PO in the ices of the comet.

#### 4.2.2 *From Solar-system bodies to primitive Earth: providing prebiotic P*

The confirmation of the presence of PO in the comet 67P/C-G has important implications for the the prebiotic chemistry that occurred on early Earth. The possible contribution of prebiotic material from comets is a long-standing topic (e.g. Chyba et al. 1990). Recent works have pointed out that comets could have contributed significantly to the chemical reservoir of our planet. O'Brien et al. (2018) claimed that ∼10% of Earth's water could have its origin in a cometary source, while Marty et al. (2017), based on ROSINA measurements of Xenon isotopes in 67P/C-G, showed that comets might provided the ∼22% of Earth's atmospheric Xe. In sight of our findings of P in 67P/C-G, we explore here the possible contribution of comets to the P reservoir on early Earth.

The amount of P in the Earth crust is 930 ppm (Yaroshevsky 2006), which means $\sim 2.6\times10^{22}$ g. However, most of this P is not available for biological processes, being locked in insoluble minerals. In the astrobiology community, there is an intense debate (known as the 'phosphate problem', see e.g. Menor-Salvan 2018) about the availability of inorganic phosphate at the dawn of our planet. Orthophosphate ($PO_4^{3-}$), which is the most common form of P on Earth, is mainly found in apatite minerals. The insolubility of these minerals locks P, which is not available for (pre)biotic chemistry. To solve this scarcity of P, alternative sources of P should be explored. One possibility comes from meteorites. It has been measured that CI chondrites, a type of stony meteorites, contain a nearly solar P abundance (Lodders 2003). This suggests that an important fraction of P likely came to the Earth in rocks. However, as mentioned before, most of this P is not easily accesible to trigger prebiotic chemistry due to low solubility in water. As a possible solution, Pasek (2008) proposed that schreibersite, $(Fe,Ni)_3P$, the major carrier of P in iron meteorites, which is more soluble in water, may be the main contributor of P in the early Earth. These authors claimed that that impacts of meteorites probably delivered between $10^{18}$ and $10^{21}$ g of P.

Another extraterrestrial possibility would be the contribution from comets. In this sense, Rubin (2019) have recently shown that most of the carbon inventory of our planet may come from comets. Similarly, the recent confirmation of PO, both in star-forming regions and in the comet 67P/C-G, suggests that it is likely that comets provided also an important contribution to the P reservoir on early Earth in the form of PO. Based on data of Xe isotopes (Marty et al. 2017), Rubin (2019) have deduced that the amount of PO that may have reached the Earth thanks to comets is between $(0.2–4)\times10^{17}$ g. Then, the fraction of PO with respect to the P from meteorites would be in the range $2\times10^{-5}$–0.4. Thus, the amount of P from comet 67P/C-G might be a negligible fraction, or maybe as important as the meteorite contribution. Given the large uncertainties in both estimates, it is difficult to draw a firm conclusion.

The predominance of PO with respect to PN might have deep implications for prebiotic and biotic chemistry, since the chemical bond between P and O is the basic building block of phosphates, which are essential elements to form large biomolecules such as DNA, RNA, phospholipids and ATP. The large amount of P in star-forming regions, and in particular in the form of an oxygen derivative, PO, implies a high availability of phosphates to be delivered to the early Earth, rather than nitrogen derivatives such as PN. This could explain why prebiotic chemistry seems to prefer PO-based compounds (Maciá et al. 1997), rather than alternative proposed paths for prebiotic chemistry based on nitrogen derivatives (PN-based; Karki et al. 2017).

## 5 SUMMARY AND CONCLUSIONS

To understand the formation of P-bearing molecules in star- and planet-forming regions, we have analysed ALMA high-resolution (∼2″) observations of PN and PO towards the massive star-forming region AFGL 5142, combined with new analysis of the data of the comet 67P/Churyumov-Gerasimenko taken with the ROSINA instrument onboard the *Rosetta* spacecraft. The ALMA maps have allowed us to study the spatial distribution and kinematics of P-bearing species for the first time in a star-forming region. We find that the emission of PN and PO comes from several spots (P-spots) associated with low-velocity gas with narrow linewidths (1–2 km $s^{-1}$) in the cavity walls of the bipolar molecular outflow powered by the central protostar. The P-bearing species are likely tracing post-shocked gas in the walls or alternatively slow shocks in the outflow wind, whose velocity is significantly lower than that of the gas along the outflow axis. There is no strong emission of P-bearing species towards the central hot molecular core or the starless cold core previously identified in AFGL 5142, nor towards

the prominent high-velocity shocks (traced by SO) along the bipolar outtflow axis. Our Local Thermodynamic Equilibrium (LTE) and non-LTE analyses show that PO is always more abundant than PN in the P-spots by factors 1.4−7.6, with only one exception (P2). We have observed an increasing trend of the PO/PN ratio with distance to the central protostar. We have found that the spatial distribution and the kinematics of PO is more similar to that of SO than that of PN. In particular, PO and PN are tracing gas at velocities shifted by ∼0.5 km $s^{-1}$ in all the spots, suggesting that they trace different layers of the cavity walls. The interpretation of our ALMA data points towards a scenario for the formation of PO and PN in which shocks are needed to sputter P from the surface of dust grains (in the form of $PH_3$), and photochemistry in the gas phase induced by UV photons from the protostar efficiently forms PO and PN in the illuminated cavity walls. If the gas of the cavity wall then collapses to form, e.g., a Sun-like star, PO can freeze-out and be trapped in the ice mantles until the formation of pebbles, rocks and ultimately comets.

The analysis of the ROSINA mass spectroscopy data has revealed a prominent peak at 46.696 Da, which is attributable to PO. PO is indeed the main carrier of P in the comet, with PO/PN>10 and $PO/PH_3$ >3.3. Similarly to other molecules ($O_2$, $S_2$ or deuterated species), there is evidence that PO was already in the cometary ices prior to the birth of the Sun. In this context, the chemical budget of the comet might have been be inherited from the natal environment of the Sun, which is thought to be a stellar cluster including also massive stars. This scenario is supported by the analysis of P-bearing molecules presented in this work, which has shown chemical similarities between the comet and the AFGL 5142 massive star-forming region, such as the predominance of PO with respect to other P-bearing species, and the good correlation between PO and SO. Finally, the dominant role of PO in the ISM and in the comet might have important implications for the supply of the budget of P on our early Earth, supporting the key role of PO-based molecules (e.g., phosphates) in prebiotic chemistry.

## ACKNOWLEDGMENTS

We thank the anonymous referee for her/his instructive comments and suggestions. This paper makes use of the following ALMA data: ADS/JAO.ALMA#2016.1.01071.S ALMA is a partnership of ESO (representing its member states), NSF (USA) and NINS (Japan), together with NRC (Canada), NSC and ASIAA (Taiwan), and KASI (Republic of Korea), in co-operation with the Republic of Chile. The Joint ALMA Observatory is operated by ESO, AUI/NRAO and NAOJ. Data from ROSINA, an instrument part of *Rosetta* mission, were used in this work. *Rosetta* is a European Space Agency (ESA) mission with contributions from its member states and NASA. We acknowledge herewith the work of the entire ESA *Rosetta* team over the last 20 years. This research utilized Queen Mary's MidPlus computational facilities, supported by QMUL Research-IT, http://doi.org/10.5281/zenodo.438045. This project has received funding from the European Union's Horizon 2020 research and innovation programme under the Marie Skłodowska-Curie grant agreement No 664931. MND acknowledges the financial support of the SNSF Ambizione grant 180079, the Center for Space and Habitability (CSH) Fellowship and the IAU Gruber Foundation Fellowship. The work by AV is supported by the Latvian Council of Science via the project lzp-2018/1-0170. MR acknowledges the support of the State of Bern, the Swiss National Science Foundation (SNSF, 200021−165869 and 200020−182418), the Swiss State Secretariat for Education, Research and Innovation (SERI) under contract number 16.0008-2, and the European Space Agency's PRODEX Programme.

## REFERENCES


Adams F. C., 2010, ARA&A, 48, 47
Agúndez M., Cernicharo J., Guélin M., 2007, ApJ, 662, L91
Agúndez M., Cernicharo J., Decin L., Encrenaz P., Teyssier D., 2014, ApJL, 790, L27
Alexander M., 1985, Chem. Phys., 92, 337
Alexander C. M. O., McKeegan K. D., Altwegg K., 2018, Space Sci. Rev., 214, 36
Altwegg K., et al., 2015, Science, 347, 1261952
Altwegg K., et al., 2016, Science Advances, 2, e1600285
Altwegg K., et al., 2017a, Philosophical Transactions of the Royal Society of London Series A, 375, 20160253
Altwegg K., et al., 2017b, MNRAS, 469, S130
Aota T., Aikawa Y., 2012, ApJ, 761, 74
Asplund M., Grevesse N., Sauval A. J., Scott P., 2009, ARA&A, 47, 481
Bachiller R., Pérez Gutiérrez M., 1997, ApJL, 487, L93
Balsiger H., et al., 2007, Space Sci. Rev., 128, 745
Bergner J. B., Oberg K. I., Walker S., Guzman V. V., Rice T. S., Bergin E. A., 2019, arXiv e-prints, p. arXiv:1910.04539
Bieler A., et al., 2015, Nature, 526, 678
Bregman J. D., Lester D. F., Rank D. M., 1975, ApJ, 202, L55
Burns R. A., et al., 2017, MNRAS, 467, 2367
Busquet G., Estalella R., Zhang Q., Viti S., Palau A., Ho P. T. P., Sánchez-Monge Á., 2011, A&A, 525, A141
Calmonte U., et al., 2016, MNRAS, 462, S253
Carpenter J. M., 2000, AJ, 120, 3139
Caselli P., et al., 2017, A&A, 603, L1
Caux E., et al., 2011, A&A, 532, A23
Ceccarelli C., Dominik C., López-Sepulcre A., Kama M., Padovani M., Caux E., Caselli P., 2014, ApJ, 790, L1
Charnley S. B., Millar T. J., 1994, MNRAS, 270, 570
Chernin L. M., Masson C. R., Fuller G. A., 1994, ApJ, 436, 741
Chyba C., Thomas P., Brookshaw L., Sagan C., 1990, Science, 249, 366
Davidsson B. J. R., et al., 2016, A&A, 592, A63
De Beck E., Kamiński T., Patel N. A., Young K. H., Gottlieb C. A., Menten K. M., Decin L., 2013, A&A, 558, A132
Drozdovskaya M. N., et al., 2018, MNRAS,
Dunning T. H., 1989, J. Chem. Phys., 90, 1007
Fagerbakke K. M., Heldal M., Norland S., 1996. pp 15–27
Fayolle E. C., et al., 2017, Nature Astronomy, 1, 703
Fernández-García C., Coggins A. J., Powner M. W., 2017, Life, 7
Fletcher L. N., Orton G. S., Teanby N. A., Irwin P. G. J., 2009, Icarus, 202, 543
Fontani F., Rivilla V. M., Caselli P., Vasyunin A., Palau A., 2016, ApJ, 822, L30
Fontani F., et al., 2017, A&A, 605, A57
Fontani F., Rivilla V. M., van der Tak F. F. S., Mininni C., Beltrán M. T., Caselli P., 2019, MNRAS, 489, 4530
Fornasier S., et al., 2016, Science, 354, 1566
Gamoke B., Neff D., Simons J., 2009, J. Phys. Chem, 113, 5677
Glassmeier K.-H., Boehnhardt H., Koschny D., Kührt E., Richter I., 2007, Space Sci. Rev., 128, 1
Goddi C., Moscadelli L., 2006, A&A, 447, 577
Goddi C., Moscadelli L., Sanna A., Cesaroni R., Minier V., 2007, A&A, 461, 1027
Goesmann F., et al., 2015, Science, 349, 020689
Grevesse N., Sauval A. J., 1998, Space Science Reviews, 85, 161
Guelin M., Cernicharo J., Paubert G., Turner B. E., 1990, A&A, 230, L9
Gulick A., 1955, Annals of the New York Academy of Sciences, 69, 309
Halfen D. T., Clouthier D. J., Ziurys L. M., 2008, ApJ, 677, L101
Hampel C., Peterson K. A., Werner H.-J., 1992, Chem. Phys. Lett., 190, 1
Hässig M., et al., 2015, Science, 347, aaa0276
Hily-Blant P., Walmsley M., Pineau Des Forêts G., Flower D., 2010, A&A, 513, A41
Hunter T. R., Testi L., Taylor G. B., Tofani G., Felli M., Phillips T. G., 1995, A&A, 302, 249
Hunter T. R., Testi L., Zhang Q., Sridharan T. K., 1999, AJ, 118, 477
Indriolo N., et al., 2015, ApJ, 800, 40
Irwin P. G. J., Parrish P., Fouchet T., Calcutt S. B., Taylor F. W., Simon-Miller A. A., Nixon C. A., 2004, Icarus, 172, 37
Jiménez-Serra I., Viti S., Quénard D., Holdship J., 2018, ApJ, 862, 128
Jorda L., et al., 2016, Icarus, 277, 257
Jura M., York D. G., 1978, ApJ, 219, 861
Kalugina Y., Lique F., Marinakis S., 2014, Phys. Chem. Chem. Phys., 16, 13500
Karki M., Gibard C., Bhowmik S., Krishnamurthy R., 2017, Life, 7, 32
Kaufman M. J., Neufeld D. A., 1996, ApJ, 456, 250
Koo B.-C., Lee Y.-H., Moon D.-S., Yoon S.-C., Raymond J. C., 2013, Science, 342, 1346
Laas J. C., Caselli P., 2019, A&A, 624, A108
Lada C. J., Lada E. A., 2003, ARA&A, 41, 57
Lamy P. L., Toth I., Davidsson B. J. R., Groussin O., Gutiérrez P., Jorda L., Kaasalainen M., Lowry S. C., 2007, Space Sci. Rev., 128, 23
Larson H. P., Treffers R. R., Fink U., 1977, ApJ, 211, 972
Le Roy L., et al., 2015, A&A, 583, A1
Lefloch B., et al., 2016, MNRAS, 462, 3937
Lichtenberg T., Golabek G. J., Burn R., Meyer M. R., Alibert Y., Gerya T. V., Mordasini C., 2019, arXiv e-prints,
Lique F., Jiménez-Serra I., Viti S., Marinakis S., 2018, Physical Chemistry Chemical Physics, 20, 5407
Liu T., et al., 2016, ApJ, 824, 31
Lodders K., 2003, ApJ, 591, 1220
Macia E., 2005, Chem. Soc. Rev., 34, 691
Maciá E., Hernández M. V., Oró J., 1997, Origins of Life and Evolution of the Biosphere, 27, 459
Marinakis S., Kalugina Y., Lique F., 2016, Eur. Phys. J. D, 70, 97
Martin-Pintado J., Bachiller R., Fuente A., 1992, A&A, 254, 315
Martín S., Martín-Pintado J., Blanco-Sánchez C., Rivilla V. M., Rodríguez-Franco A., Rico-Villas F., 2019, arXiv e-prints, p. arXiv:1909.02147
Marty B., et al., 2017, Science, 356, 1069
Menor-Salvan C., 2018, Prebiotic Chemistry and Chemical Evolution of Nucleic Acids. Vol. 35
Milam S. N., Halfen D. T., Tenenbaum E. D., Apponi A. J., Woolf N. J., Ziurys L. M., 2008, ApJ, 684, 618
Mininni C., Fontani F., Rivilla V. M., Beltrán M. T., Caselli P., Vasyunin A., 2018, MNRAS, 476, L39
Müller H. S. P., Thorwirth S., Roth D. A., Winnewisser G., 2001, A&A, 370, L49
Müller H. S. P., Schlöder F., Stutzki J., Winnewisser G., 2005, Journal of Molecular Structure, 742, 215
O'Brien D. P., Izidoro A., Jacobson S. A., Raymond S. N., Rubie D. C., 2018, Space Science Reviews, 214, 47
Padovani M., Marcowith A., Hennebelle P., Ferrière K., 2016, A&A, 590, A8
Pasek M. A., 2008, Proceedings of the National Academy of Sciences, 105, 853
Pasek M. A., Lauretta D. S., 2005, Astrobiology, 5, 515
Pfalzner S., et al., 2015, Phys. Scr., 90, 068001
Pineau des Forets G., Roueff E., Schilke P., Flower D. R., 1993, MNRAS, 262, 915
Podio L., Lefloch B., Ceccarelli C., Codella C., Bachiller R., 2014, A&A, 565, A64
Podio L., et al., 2015, A&A, 581, A85
Powder M. W., Gerland B., Sutherland J., 2009, Nature, 459, 239
Qiu K., et al., 2008, ApJ, 685, 1005
Redfield A., 1958, American Scientist, 46, 205
Ridgway S. T., Wallace L., Smith G. R., 1976, ApJ, 207, 1002
Rivilla V. M., Martín-Pintado J., Sanz-Forcada J., Jiménez-Serra I., Rodríguez-Franco A., 2013a, MNRAS, 434, 2313
Rivilla V. M., Martín-Pintado J., Jiménez-Serra I., Rodríguez-Franco A., 2013b, A&A, 554, A48
Rivilla V. M., Jiménez-Serra I., Martín-Pintado J., Sanz-Forcada J., 2014, MNRAS, 437, 1561
Rivilla V. M., Fontani F., Beltrán M. T., Vasyunin A., Caselli P., Martín-Pintado J., Cesaroni R., 2016, ApJ, 826, 161

Rivilla V. M., et al., 2018, MNRAS, 475, L30
Rivilla V. M., Beltrán M. T., Vasyunin A., Caselli P., Viti S., Fontani F., Cesaroni R., 2019, MNRAS, 483, 806
Rubin M. e. a., 2019, ACS Earth and Space Chemistry
Rubin M., et al., 2015, Science, 348, 232
Rubin M., et al., 2019, MNRAS, 489, 594
Schöier F. L., van der Tak F. F. S., van Dishoeck E. F., Black J. H., 2005, A&A, 432, 369
Schwartz A. W., 2006, Phil. Trans. of the Royal Soc. Biol. Sci., 361, 1743
Smith M. D., Rosen A., 2005, MNRAS, 357, 1370
Sousa-Silva C., Seager S., Ranjan S., Petkowski J. J., Zhan Z., Hu R., Bains W., 2019, arXiv e-prints, p. arXiv:1910.05224
Spezzano S., Caselli P., Bizzocchi L., Giuliano B. M., Lattanzi V., 2017, A&A, 606, A82
Stein S., 2016, National Institute of Standards and Technology, Gaithersburg, MD
Taquet V., Wirström E. S., Charnley S. B., 2016, ApJ, 821, 46
Tenenbaum E. D., Woolf N. J., Ziurys L. M., 2007, ApJL, 666, L29
Toboła R., Kłos J., Lique F., Chałasiński G., Alexander M. H., 2007, A&A, 468, 1123
Turner B. E., Bally J., 1987, ApJL, 321, L75
Turner B. E., Tsuji T., Bally J., Guelin M., Cernicharo J., 1990, ApJ, 365, 569
Van der Tak F. F. S., Black J. H., Schöier F. L., Jansen D. J., van Dishoeck E. F., 2007, A&A, 468, 627
Vincent J.-B., et al., 2016, MNRAS, 462, S184
Wakelam V., Herbst E., 2008, ApJ, 680, 371
Watts J. D., Gauss J., Bartlett R. J., 1993, J. Chem. Phys., 98, 8718
Weisstein E. W., Serabyn E., 1994, Icarus, 109, 367
Werner H.-J., Knowles P. J., Knizia G., Manby F. R., Schütz M., et al., 2018, MOLPRO, version 2018.1, a package of ab initio programs
Williams H. L., Mass E. M., Szalewicz K., Jeziorski B., 1995, J. Chem. Phys., 103, 7374
Yamaguchi T., et al., 2011, Publications of the Astronomical Society of Japan, 63, L37
Yaroshevsky A. A., 2006, Geochemistry International, 44, 48
Zhang Q., Hunter T. R., Sridharan T. K., Ho P. T. P., 2002, ApJ, 566, 982
Zhang Q., Hunter T. R., Beuther H., Sridharan T. K., Liu S.-Y., Su Y.-N., Chen H.-R., Chen Y., 2007, ApJ, 658, 1152
Ziurys L. M., 1987, ApJL, 321, L81
Ziurys L. M., Schmidt D. R., Bernal J. J., 2018, ApJ, 856, 169

## APPENDIX A: AFFILIATIONS

[1] INAF-Osservatorio Astrofisico di Arcetri, Largo Enrico Fermi 5, I-50125, Florence, Italy
[2] Center for Space and Habitability, University of Bern, Gesellschaftsstrasse 6, CH-3012 Bern, Switzerland
[3] Physikalisches Institut, University of Bern, Sidlerstrasse 5, CH-3012 Bern, Switzerland
[4] Max-Planck-Institute for Extraterrestrial Physics, Garching, Germany
[5] SRON Netherlands Institute for Space Research, Landleven 12, 9747 AD Groningen, The Netherlands
[6] Kapteyn Astronomical Institute, University of Groningen, The Netherlands
[7] Ural Federal University, Ekaterinburg, Russia
[8] Visiting Leading Researcher, Engineering Research Institute 'Ventspils International Radio Astronomy Centre' of Ventspils University of Applied Sciences, Inženieru 101, Ventspils LV-3601, Latvia
[9] LOMC – UMR 6294, CNRS-Université du Havre, France
[10] School of Health, Sport & Bioscience, University of East London, Stratford Campus, Water Lane, London E15 4LZ, UK
[11] Department of Chemistry and Biochemistry, School of Biological and Chemical Sciences, Queen Mary University of London, Joseph Priestley Building, Mile End Road, London E1 4NS, UK
[12]ESO/European Southern Observatory, Karl Schwarzschild str. 2, D-85748, Garching, Germany
[13]Excellence Cluster "Universe", Boltzmann str. 2, D-85748 Garching bei Muenchen, Germany
[14] The ROSINA team: H. Balsiger[15], J. J. Berthelier[16], J. De Keyser[17], B. Fiethe[18], S. A. Fuselier[19], S. Gasc[15], T. I. Gombosi[20], T. Sémon[15], C. -y. Tzou[15]; [15]Physikalisches Institut, University of Bern, Sidlerstrasse 5, CH-3012 Bern, Switzerland. [16]LATMOS 4 Avenue de Neptune, F-94100 SAINT-MAUR, France. [17]Royal Belgian Institute for Space Aeronomy (BIRA-IASB), Ringlaan 3, B-1180 Brussels, Belgium. [18]Institute of Computer and Network Engineering (IDA), TU Braunschweig, Hans-Sommer-Strasse 66, D-38106 Braunschweig, Germany. [19]Space Science Division, Southwest Research Institute, 6220 Culebra Road, San Antonio, TX 78228, USA. [20]Department of Atmospheric, Oceanic and Space Sciences, University of Michigan, 2455 Hayward, Ann Arbor, MI 48109, USA.

## APPENDIX B: HYPERFINE EXCITATION OF PO BY HE

Collisional cross sections for the excitation of PO($^2\Pi$) by collisions with He atoms have been computed recently by Lique et al. (2018). In the calculations, the hyperfine structure of the PO radical was taken into account. The $^{31}$P nucleus possesses a non-zero nuclear spin ($I$ = 1/2), which couples with $\vec{j}$ (the rotational momentum) resulting in a splitting of each Λ-doublet level into two hyperfine levels. The hyperfine levels are labeled by $F$, which is the quantum number of the total angular momentum $\vec{F} = \vec{j} + \vec{I}$, and takes values between $|j - I|$ and $|j + I|$.

The cross-section calculations were based on a new PO–He potential energy surface (PES) described in detail in Lique et al. (2018). Briefly, *ab initio* calculations of the PES of the PO–He van der Waals complex were carried out in the open-shell partially spin-restricted coupled cluster approach at the single, double and perturbative triple excitations [UCCSD(T)] (Hampel et al. 1992; Watts et al. 1993) level of theory using the `MOLPRO` 2010 package (Werner et al. 2018). The calculations were performed using the augmented correlation-consistent triple zeta (aug-cc-pVTZ) basis set (Dunning 1989) augmented with bond functions defined by Williams et al. (1995).

Close-coupling quantum scattering calculations were carried out using the HIBRIDON[8] program which provided integral cross sections. Nuclear spin free $S^J(F_i j\varepsilon l; F_i' j'\varepsilon' l')$ scattering matrices between the PO rotational levels were obtained following the standard formalism for collisions of diatomic open-shell molecules with atoms (Alexander 1985; Kalugina et al. 2014). In the above notation, $F_i$ denotes the spin-orbit manifold, $l$ the orbital angular momentum quantum numbers, and $J$ the total angular momentum ($\vec{J} = \vec{j} + \vec{l}$). The symbols $\varepsilon$, $\varepsilon'$ label the Λ-doublet level which can be either $e$ or $f$. Hyperfine cross sections for transitions from $F_i j\varepsilon F$ to $F_i' j'\varepsilon' F'$

[8] The HIBRIDON package (version 4.4) was written by M. H. Alexander, D. E. Manolopoulos, H.-J. Werner, B. Follmeg, and P. Dagdigian with contributions by D. Lemoine, P. F. Vohralik, G. Corey, R. Gordon, B. Johnson, T. Orlikowski, A. Berning, A. Degli-Esposti, C. Rist, B. Pouilly, J. Kłos, Q. Ma, G. van der Sanden, M. Yang, F. de Weerd, S. Gregurick, and F. Lique; `http://www2.chem.umd.edu/groups/alexander/`

were obtained using a recoupling technique (Marinakis et al. 2016). Details on the calculations were provided in Lique et al. (2018).

Here, from the calculated cross sections of Lique et al. (2018), we have obtained the corresponding thermal rate coefficients at temperature $T$ by averaging over the collision energy ($E_c$):

$$k_{\alpha\rightarrow\beta}(T) = \left(\frac{8}{\pi\mu k_B^3 T^3}\right)^{\frac{1}{2}} \times \int_0^\infty \sigma_{\alpha\rightarrow\beta}\, E_c\, e^{-\frac{E_c}{k_B T}}\, dE_c \quad \text{(B1)}$$

where $\sigma_{\alpha\rightarrow\beta}$ is the cross section, $\mu$ is the reduced mass of the system and $k_B$ is Boltzmann's constant. Calculations up to 960 $cm^{-1}$ allowed determining rate coefficients from 10 to 150 K. The first 116 hyperfine levels were considered in the calculations.

This paper has been typeset from a TEX/LATEX file prepared by the author.